Original Contribution

Kurume Medical Journal, 57, 1-8, 2010

Effects of Angiotensin Receptor Blocker and Calcium Channel Blocker on Experimental Abdominal Aortic Aneurysms in a Hamster Model

YUKIO HOSOKAWA

Department of Surgery, Kurume University School of Medicine, Kurume 830-0011, Japan

Received 21 October 2009, accepted 22 January 2010

Summary: Remodeling in the abdominal aortic wall results in abdominal aortic aneurysm (AAA) formation. Many patients with AAA are prescribed antihypertensive drugs. However, the effects of antihypertensive drugs other than their effects on blood pressure control are rarely reported. In this study, we investigated the effects of these drugs on changes in the levels of matrix metalloproteinases (MMPs) and on AAA formation. Experimental AAAs were created in a hamster model by wrapping the abdominal aorta with elastase gauze. Olmesartan medoxomil (angiotensin Ⅱ receptor antagonist) or azelnidipine (calcium channel antagonist) was administered to the hamsters and then we evaluated the aortic diameter, performed histological analysis, and analyzed the production of MMP-2 and MMP-9 by gelatin zymography. The expansion rate of the aortic diameter was smaller in both treatment groups than in the control group. Elastica van Gieson (EVG) staining showed structural preservation of elastin lamellae in both treatment groups. The active MMP-9 level decreased in both the olmesartan group and the azelnidipine group. Reducing MMP-9 production is important for suppression of AAA formation. Both olmesartan medoxomil and azelnidipine decreased MMP-9 activity, which suppressed degradation of the MMPs and inhibited AAA formation. There are different cascades that determine the production of MMP-9.

Key words abdominal aortic aneurysm, matrix metalloproteinase-9, matrix metalloproteinase-2, angiotensin Ⅱ receptor antagonist, olmesartan medoxomil

INTRODUCTION

The developmental mechanism of aortic aneurysms has not yet been clarified. The goal of treatment is to prevent aneurysmal expansion and rupture. Most current theories on the mechanisms responsible for the formation of an abdominal aortic aneurysm (AAA) hold that degradation of the extracellular matrix (ECM) in the arterial wall, especially elastin, results in aneurysmal dilatation [1-3]. Thomas et al. [4] reported that deletion of $p47^{phox}$ attenuates angiotensin Ⅱ-induced aneurysmal formation in an apolipoprotein E-deficient mice model, suggesting that NADPH oxidase plays a critical role in AAA formation.

Histologically, there is significant disruption of medial elastin or complete disorganization of the few remaining medial elastin elements after chronic inflammation within the outer aortic wall [5-7]. The pathophysiology of an aortic aneurysm includes aortic atherosclerosis, chronic inflammation within the outer aortic wall, and an imbalance between the production and degradation of structural ECM proteins (White et al., 1993) [8-11].

Increased expression of matrix metalloproteinases (MMPs) is observed in aneurysm tissue. When inflammation occurs in the normal aorta, NF-κB activates transcription of various kinds of genes. This phenomenon transactivates the gene transcription of MMP-9, following which MMP-9 activity leads to the degradation of ECMs and aneurysm formation [12-13]. MMPs,

Correspondence to: Yukio Hosokawa, MD, Department of Surgery, Kurume University School of Medicine, 67 Asahi-machi, Kurume 830-0011, Japan. Tel: +81-942-35-3311 Fax: +81-942-35-8967 E-mail: getageta@med.kurume-u.ac.jp

Abbreviations: AAA, abdominal aortic aneurysm; ACE, angiotensin Ⅱ-forming enzyme; EAD, external aortic diameter; ECM, extracellular matrix; MMP, matrix metalloproteinases.

which disintegrate ECM proteins in aortic tissue, are a family of zinc enzymes present in normal healthy individuals that participate in cell turnover and growth. It is generally thought that MMP-2 and MMP-9 in particular play important roles in the aneurysmal wall remodeling process by degrading extracellular matrix proteins such as elastin and collagen, both of which are needed to maintain the structural integrity and mechanical properties of the aortic tissue [11-14].

It has become clear that angiotensin Ⅱ and chymase, which is a serine protease, play roles in the cascade of MMP-9 activation [5,7]. Angiotensin Ⅱ plays an important role in the activation of inflammatory reactions in atherosclerosis (Miyazaki et al., 1999) [16-17]. Angiotensin Ⅱ is generated from angiotensin I by two distinct types of angiotensin Ⅱ-forming enzyme (ACE) and chymase in human cardiovascular tissues (Takai et al., 1999) [16-17]. It has been reported that the ratio of chymase-dependent angiotensin Ⅱ-forming activity to total angiotensin Ⅱ-forming activity is significantly higher in aneurysmal aortas than in normal aortas (Ihara et al., 1999) [16,18]. It has also been reported that chymase activity was significantly increased in human AAA, and that accumulated chymase-positive mast cells were observed in the media and adventitia (Nishimoto et al., 2002) [19]. A specific chymase inhibitor, 2-(5-formyamino-6-oxo-2 phenyl-1, 6-dihydropyrmidine-1-yl) N-[{3, 4-dioxo-1-phenyl-7-} 2-pyridyloxy]}-2heptyl] acetamide (NK3201), has been shown to suppress the development of AAA in hamsters (Tsunemi et al., 2004) [16]. Meanwhile, Yokokura et al. (2007) reported that a new calcium antagonist, azelnidipine, may act via an anti-inflammatory mechanism in a rat AAA model, thus resulting in inhibition of aortic expansion. They showed that azelnidipine appeared to influence the inflammatory oxidative response seen in the rat AAA model while also decreasing the MMP-2 and MMP-9 levels [11]. Azelnidipine has been described as an important agent in preventing vascular remodeling [21]. For these reasons, we decided to use azelnidipine in the present study.

First, we prepared an elastase-gauze wrapped hamster model of AAA in which an isolated segment of the infrarenal aorta is wrapped with porcine pancreatic elastase in order to stimulate inflammation of the outer aortic wall. Next, we measured MMP-2 and MMP-9 activity and aortic diameter in an experimental hamster model that has the same chymase activity as humans, and evaluated the effectiveness of olmesartan medoxomil, which we use on a daily basis to suppress hypertension. We also compared it with azelnidipine, a calcium antagonist that is also routinely used.

The goals of these experiments were to examine how ARB and CCB can stabilize aortic aneurysms in an animal model.

MATERIALS AND METHODS

Drugs

We evaluated the effectiveness of an angiotensin Ⅱ receptor 1 antagonist olmesartanmedoxomil, (5-methyl-2-oxo-1,3-dioxolen-4-yl)methyl4-(1-hydroxy-1-methylethyl)-2-propyl-1-{[2'-(1H-tetrazol-5-yl)-1,1'-biphenyl-4-yl]methyl}-1H-imidazole-5-carboxylate (CS-866) and a calcium channel blocker azelnidipine, (±)-3-(1-diphenylmethylazetidin-3-yl) 5-isopropyl2-amino-1,4-dihydro-6-methyl-4-(3-nitrophenyl)-3,5-pyridipinedicarboxylate (CS-905). These drugs were provided by Daiichi Sankyo laboratories.

Animals

Male Syrian hamsters weighting 170 to 220 g were obtained from KYUDO Co., LTD. (Fukuoka, Japan). The hamsters were fed regular hamster chow, had free access to tap water, and were housed in a temperature, humidity, and light-controlled room. The animals were cared for in accordance with the Kurume University Guide for the Care and Use of Experimental Animals.

Surgical procedure

In the first part of the study, the animals were anesthetized with 6% pentobarbital (Dainippon Laboratories, Osaka, Japan) (0.1 mL/100 g body weight), and a laparotomy was performed under sterile conditions. The infrarenal aorta was isolated from the level of the left renal vein to the aortic bifurcation. The mesenteric artery and all lumbar arteries arising from the infrarenal aorta were ligated, and the external aortic diameter (EAD) was measured. The isolated segment of the aorta was then wrapped with porcine pancreatic elastase (Aqueous suspension, Nacalai Tesque, Kyoto, Japan) (180 U/mL). Aortic wrapping was performed for 60 min. The EAD after wrapping was measured. The wound was closed and the animals were kept in individual cages. The animals were euthanized by a lethal overdose of pentobarbital at a predetermined day. Immediately before the hamsters were euthanized, the abdominal aorta was measured under physiologic conditions. The control group was treated with saline without elastase.

In the second part of the study, in order to investi-

gate the effects of an ARB and a CCB, olmesartan medoxomil (5 mg/kg once daily), azelnidipine (3 mg/kg once daily) or a placebo was orally administered to the hamsters beginning after application of the elastase and then throughout the experiments. In the placebo treated group, hamsters were administered the same volume of 0.5% carboxymethyl cellulose. The animals were euthanized by a lethal overdose of pentobarbital on the 21st day after the procedure. We assessed the EAD and the expression levels of MMP-2 and MMP-9 in the abdominal aorta after the procedure. EAD was measured immediately after gauze wrapping (W) and before euthanasia (E). The increase from the value at gauze wrapping was calculated as follows: (E-W)× 100/W (%). Aneurysmal formation was defined as an increase in EAD >50%. We measured blood pressure in the experimental hamsters. We confirmed that the medicines did not cause a decrease of blood pressure. Blood pressure was the mean of 10 consecutive measurements by tail cuff technique using a MK200 (Muromachi, Tokyo, Japan).

Histological analysis

The aortic segments were fixed in 10% formalin overnight and embedded in paraffin. Sections (5 μm thick) were cut from each block. The slices were stained with hematoxylin-eosin (HE) and Elastica van Gieson (EVG) stains.

Gelatin zymography

The tissue specimens were thawed over ice and homogenized in the buffer. The homogenates were centrifuged and dialyzed. Samples containing an equal amount of protein were loaded on Novex Zymogram Gels (Invitrogen) under nonreducing conditions (125 mM Tris–HCl, 2% SDS, 10% glycine, 20 mM DTT, 0.01 bromophenol blue, pH 6.8). The gels were electrophoresed in the presence of 10% sodium dodecyl sulfate (SDS)-Novex Zymogram Gels (Invitrogen) with a constant current of 150 V at 25 mA/gel with running buffer (25 mM Tris, 192 mM glycine, 10% SDS). After electrophoresis, the gels were then washed three times in 2.5% Triton-X-100 (Sigma, St. Louis, MO, USA) for 30 min to remove the SDS (Bio-Rad Laboratories, Hercules, CA, USA). The gels were incubated for 24 hrs at 37 °C and then stained with 0.2% Coomassie brilliant blue (Sigma, St. Louis, MO, USA) in 5% acetic acid (Nacalai Tesque, Kyoto, Japan) and 10% ethanol (Nacalai Tesque). The molecular weight of each band was estimated in comparison to the position of known molecular weight standards (VENUS Markers, Pre-Stained, Nacalai Tesque). The gelatinolytic activity was indicated by a clear zone of lysis against the dark background staining of the substrate protein in the gel. The gelatinolytic activity was quantified by densitometry using LumiImager software (Roche, Mannheim, Germany) and the results are expressed as artificial Boehringer Light Units (BLU). Experiments were performed in duplicate.

Statistical analysis

All numerical data shown in the text are expressed as the mean ± SD. Significant differences among the mean values of multiple groups were evaluated by one-way analysis of variance (ANOVA) followed by a post-hoc analysis (the Tukey-Kramer test or the Dunnett test using a commercially available software program, Stat Mate). $p<0.05$ was used as the threshold to indicate a statistically significant difference.

RESULTS

Expansion rate of aortic diameter

Five hamsters each were sacrificed 7, 14, 21, and 28 days after the operation. Among the four groups, there was a statistically significant increase in the rate of expansion in aortic diameter in the 21-day group (mean, 68.7±5.5%) ($p<0.01$) (Fig. 1), leading us to conclude that the maximum aortic inflammatory change with elastase is on postoperative day 21. Therefore, in the second part of the experiment, we sacrificed another 20 hamsters that survived 21 days after elastase wrapping in order to evaluate the inhibition of aortic aneurysmal formation by olmesartan medoxomil or azelnidipine.

There was a statistically significant increase in the

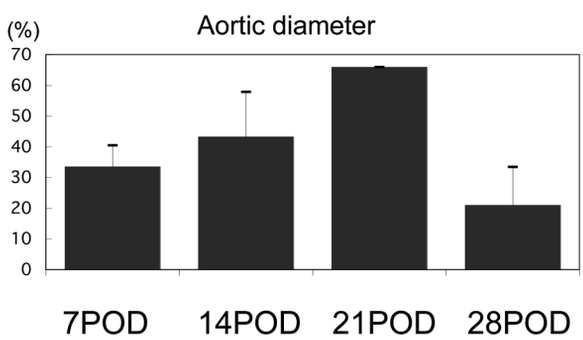

Fig. 1. Aortic diameter expansion rate of the experimental AAA hamsters on postoperative day (POD) 7,14,21,28. There was a statistically significant increase in the expansion rate of aortic diameter in the 21day group (mean, 68.7±5.5%) ($p<0.01$). (n=8)

EAD expansion rate of the control group (55.6±12.7%) compared with the olmesartan group (6.2±9.1%) and the azelnidipine group (12.2±11.6%) ($P<0.01$ for both) (Fig. 2).

Sphygmomanometry

There was no difference in systolic pressure between the treated and untreated groups. In the treatment groups, systolic pressure did not change during the observation period (Fig. 3).

Histological analysis

HE staining showed that inflammatory cells such as mature granulocytes and monocytes decreased in both the media and adventitia of the aneurysmal aortic segments in both the olmesartan group and the azelnidipine group compared with the control group. The intensity of cell infiltration in the olmesartan group and the azelnidipine group was less than that in the control group. EVG staining showed extensive degradation of the elastic lamellae in the aneurysmal aortic tissues. Treatment with olmesartan or azelnidipine showed slightly better structural elastin lamellae compared with the control group. (Fig. 4 and Fig. 5).

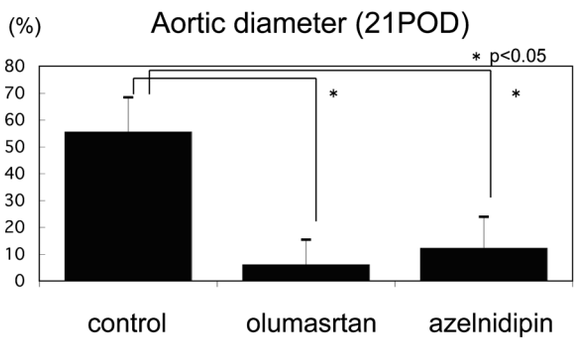

Fig. 2. The relative of aortic diameter expansion rate between immediately before elastase gauze wrapping, and 21POD among the control hamsters, olumesartan treated hamsters, and azelnidipine treated hamsters. Aortic diameter expansion rate decreased 88.8% and 78.0% respectively in the olumesartan-treated hamsters and azelnidipine treated hamsters as compare with control group. (n=5)

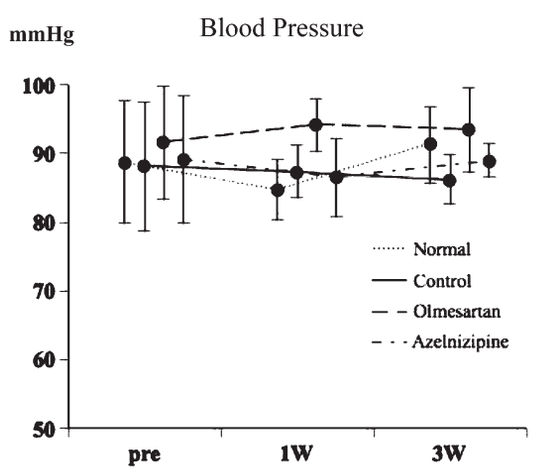

Fig. 3. Systolic blood pressure. Group N, normal group; Group C, control group; Group O, olumesartan treated group; Group A, azelnidipine treated group. (n=5)

Gelatin zymography

We assessed the proteolytic activity of MMP-2 and MMP-9 using gelatin zymography. (Fig. 6-a) Each band corresponds to a 92 kDa for doublet pro-MMP-9, an 84 kDa for active MMP-9, a 72 kDa for doublet pro MMP-2, and a 62 kDa for active MMP-2. The levels of pro MMP-2, active MMP-2, pro MMP-9, and active MMP-9 in the control group were 2.52, 1.63, 3.11, and 4.77 times, respectively, higher than those in the normal group ($p<0.05$ for each). In the olmesartan medoxomil group, the levels of pro MMP-9 and active MMP-9 decreased by 51.7% and 48.0% compared with the control group, respectively. In the azelnidipine group, these levels decreased by 33.2% and 45.2% compared with the control group, respectively. However, MMP-2 levels decreased only slightly in the olmesartan medoxomil and azelnidipine groups. (Fig. 6-b)

DISCUSSION

The results of the present study indicate that MMP-2 and MMP-9 were increased in the present experimental AAA formation model. We believe that MMP-9 was decreased by the treatment with ARB or CCB in our hamster AAA model.

An increase of MMP activity in AAA formation with elastin degradation has been reported. The increase of elastinolytic activity in aneurysmal tissue has recently been ascribed to the increases in MMP-2 and MMP-9 activities. In our experiments, pro MMP-2, active MMP-2, pro MMP-9, and active MMP-9 levels in the control group (no medication group) were 2.52, 1.63, 3.11, and 4.77 times higher, respectively, than those in the normal group. (Fig. 6-b)

Both olmesartan medoxomil and azelnidipine reduced the extent of aneurysmal expansion compared with the control group. The hamsters treated with olmesartan medoxomil or azelnidipine exhibited superior elastin fiber preservation compared with the control group. Elastin destruction takes place only in areas

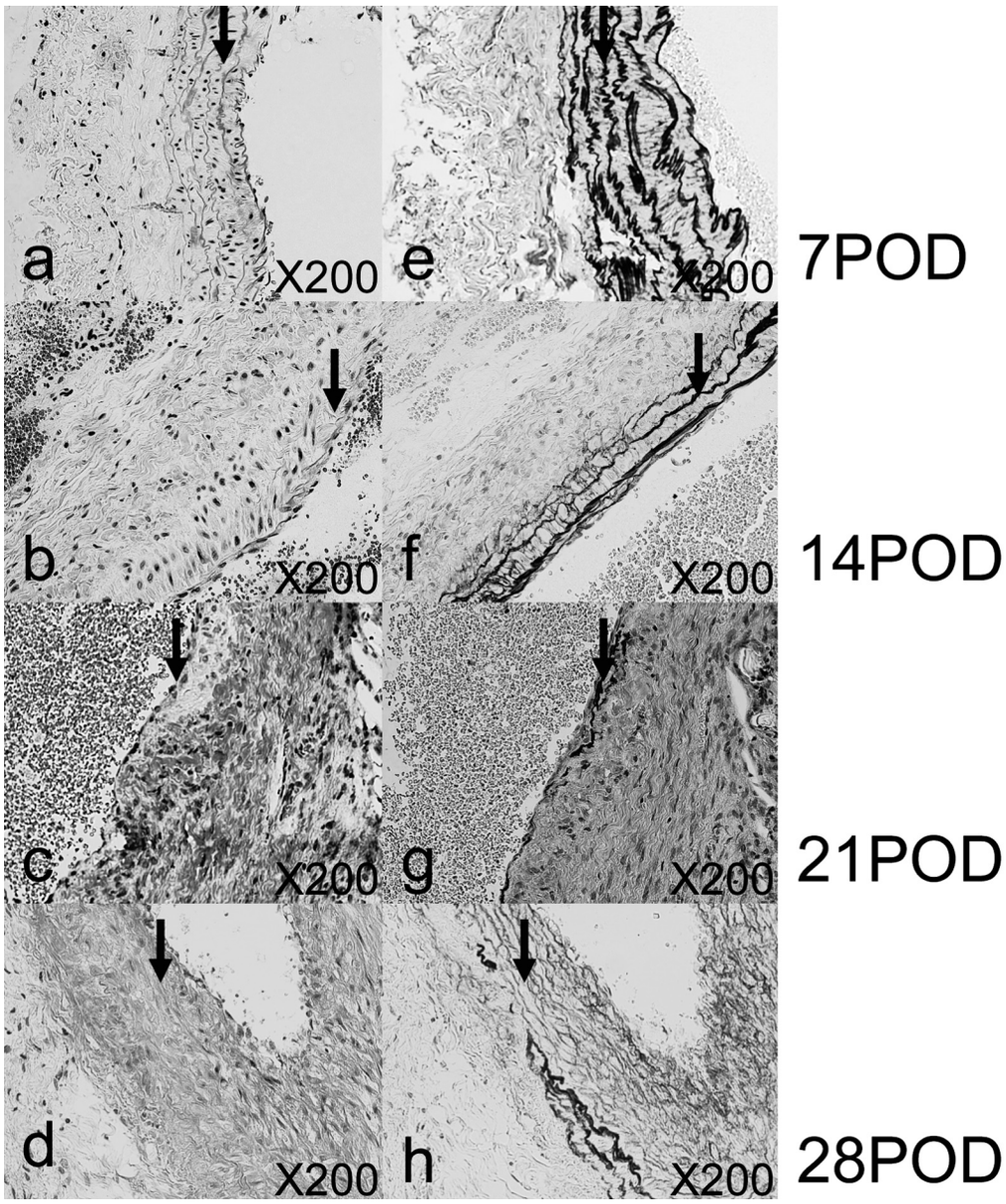

Fig. 4a-h: Typical photographs of the aortas in experimental AAA formation in hamsters (7POD, 14POD, 21POD, 28POD) a~d ; H&E stain, e~h; EVG stain. ↓ ; Media.

where inflammation has occurred. After wrapping the aorta with elastase gauze, an inflammatory response develops in the hamster aortic wall.

A significantly higher production of MMP-9 was found in the walls of aneurysms. In our experiments, pro and active MMP-9 levels in the olmesartan medoxomil group and in the azelnidipine group decreased by 51.7% and 33.2%, respectively ($p<0.05$) (Fig. 6-b). However, the MMP-2 levels decreased only slightly. MMP-9 is a key enzyme in matrix component degradation, suggesting a role in matrix remodeling. Known substrates of MMP-9 include collagen fragments, gelatin, elastin, aggrecan, versican, and fibronectin. Some of these have important roles in the remodeling process. MMP-9 has been implicated in angiogenesis and apoptosis [10,27,28]. On the basis of previous results, we believe that MMP-9 activity leads to a progressive destruction of the arterial wall extracellular matrix and subsequent aneurysmal formation [1].

Olmesartan medoxomil suppresses the production of active MMP-9 by inhibiting angiotensin Ⅱ and NF-κB activation. Recently, Naito et al. reported that azelnidipine inhibited 7-ketocholesterol or tumor necrosis factor-α (TNF-α), which induce NF-κB activation and vascular cell adhesion molecule-1 (VCAM-1) expression. In any case, both olmesartan medoxomil and azel-

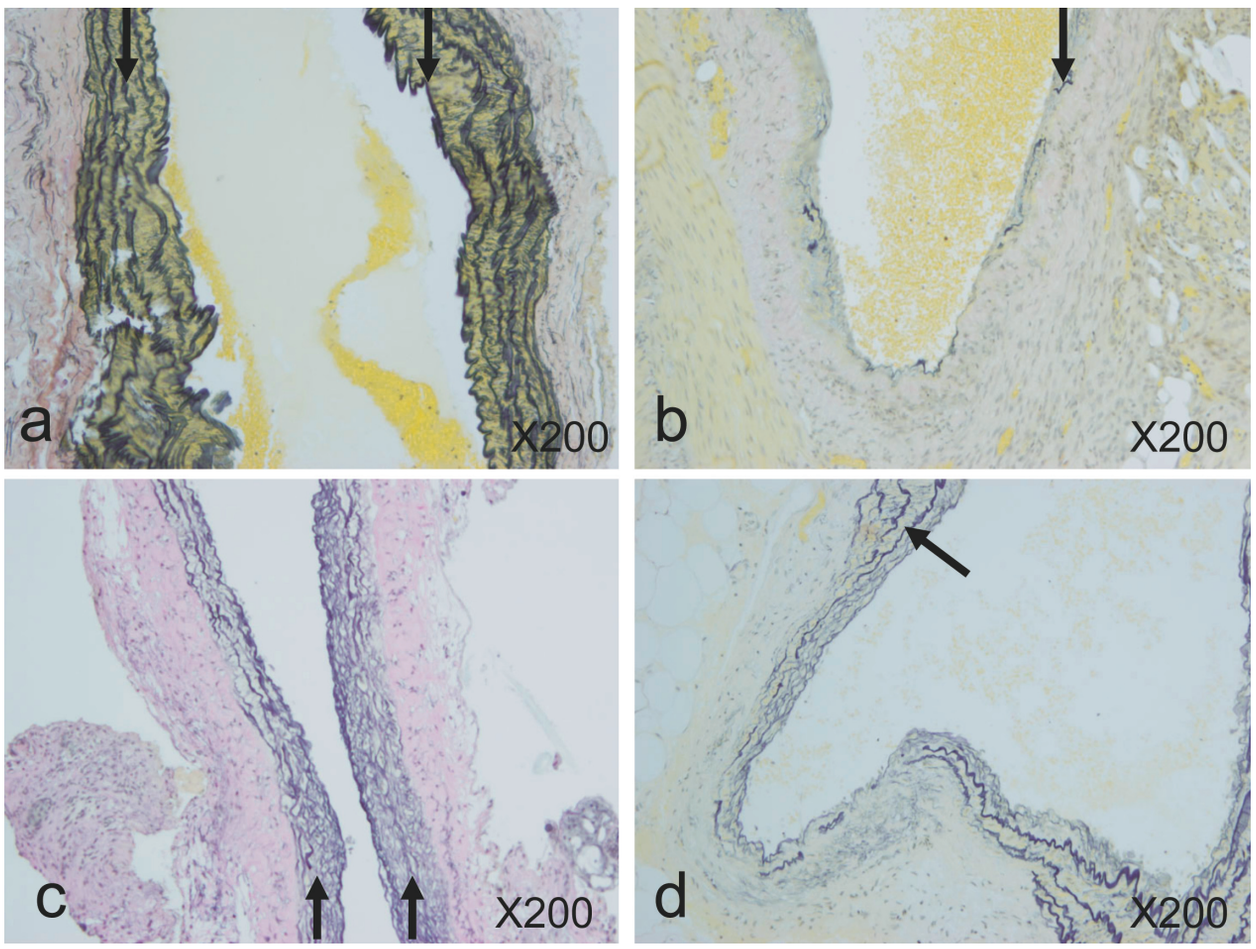

Fig. 5a-d: The effect of olumesaltan and azelnidipine on the histology of experimental AAA. Transverse sections were stained with EVG. a; Normal abdominal aorta, b; Control group, c; olumasartan group, d; azelnidipine group. The destruction of elastin lamellae were observed in the control group. But, the destruction of elastin lamellae in the olumasartan group and the azelnidipine group were less than in the control group. ↓ ; Media.

nidipine reduce active MMP-9 by suppressing the production of NF-κB [21-23].

In the present experiment, olmesartan medoxomil and azelnidipine treatment each suppressed the expansion of AAA to a similar extent in comparison with the control group. Pathological analysis revealed both groups showed an approximately equal inhibition of the destructive effect on elastic fibers. Zymography revealed similar decreases of active MMP-9 in both groups. On the other hand, Yokokura et al. reported that azelnidipine suppressed AAA formation by decreasing MMP-9 and MMP-2 activities in a rat model which did not have the same chymase activity as humans. In the present hamster model which has the same chymase cascade as humans, olmesartan medoxomil and azelnidipine suppressed AAA formation by decreasing MMP-9 activity. In the rat model that did not have a chymase cascade, azelnidipine suppressed AAA formation by decreasing MMP-9 and MMP-2 activities. These two agents both suppress development of AAA by deactivating NF-κB.

ACKNOWLEDGMENTS: We are grateful to Professor T. Ueno, Dr. T. Nakamura, Dr. R. Yamagishi, Dr. S. Takai, Dr. T. Ueda, and T. Nakashima for their advice and technical assistance. This study was supported by Sankyo Laboratories and the Kurume University Research Center for Innovative Cancer Therapy.

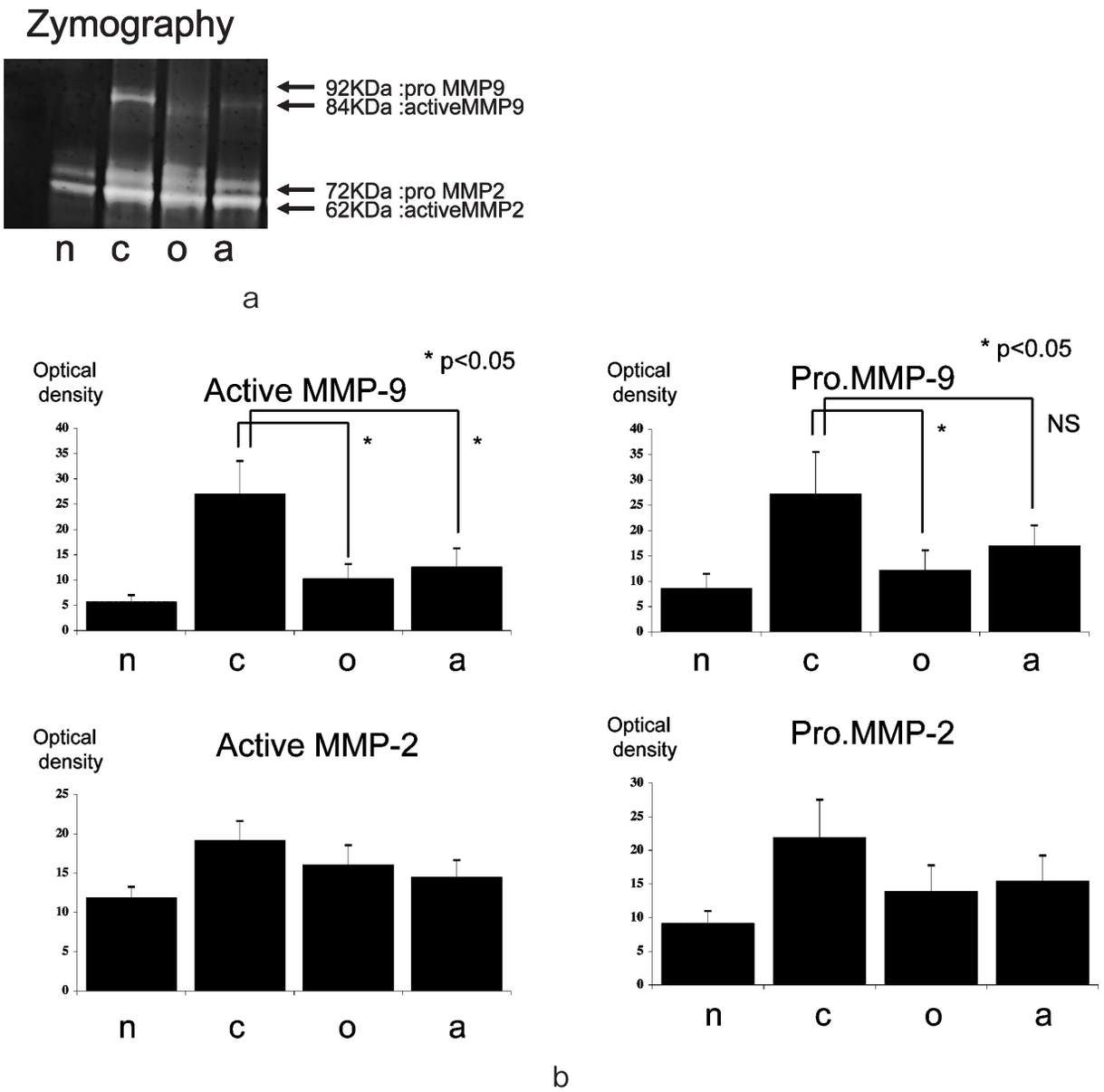

Fig. 6a-b. a. Gelatin zymography of aortic segments in normal hamsters (N), control hamsters (C), olumasartan-treated hamsters (O), and azelnidipine-treated hamsters (A). b. The densitometery levels of pro MMP-2, active MMP-2, pro MMP-9, and active MMP-9 in the control group were 2.52, 1.63, 3.11, and 4.77 times, respectively, higher than those in the normal group. (n=5)

REFERENCES

1. James RE, Bonnie FK, David PF, Jerry RY, and David JC. Expression of Matrix Metalloproteinases and TIMPs in Human Abdominal Aortic Aneurysms. Annals of Vascular Surgery 1998; 12:221-228.
2. Rizzo RJ, McCarthy WJ, and Dixit SN. Collagen types and matrix protein content in human abdominal aortic aneurysms. J Vasc Surg 1989; 10:365-373.
3. Tilson MD. Histochemistry of aortic elastin in patients with nonspecific abdominal aortic aneurysmal disease. Arch Surg 1988; 123:503-505.
4. Mnesh T, Dan G, Michel LM, Francis JM, Alan D et al. Deletion of p47 ^{phox} attenuates angiotensin Ⅱ-induced abdominal aortic aneurysm formation in apolipoprotein E-deficient mice. Circulation 2006; 114:404-413.
5. Tsunemi K, Takai T, Nishimoto M, Denan Jin, Sakaguchi M et al. The Role of Chymase in aortic aneurysm: the Effect of Chymase inhibitor on the Suppression of the progression of Aortic Aneurysm. J Jpn Coll Angiol 2003; 43:749-754.
6. Watanabe T, Sawai T, Sato A, and Satomi S. A mapping analysis of the distribution of MMP-2 and MMP-9 in the wall of abdominal aortic aneurysms and correlation with

the disruption of elastic fibers. Jpn J Vasc Surg 2000; 9:539-544. (in Japanese)
7. Miyazaki M, and Takai S. Role of chymase on vascular proliferation. J Renin Angiotensin Aldesteron Syst 2000; 1:23-26.
8. White JV, Haas K, and Phillips S. Adventitial elastolysis is a primary event in aneurysmal formation. J Vasc Surg 1993; 17:371-381.
9. Freestne T, Turner RJ, and Coady A. Inflammation and matrix metalloproteinases in the enlargeing abdominal aortic aneurysm. Arterioscler Thromb Vasc Biol 1995; 15:1145-1151.
10. Pugin J, Verghese G, and Widmer MC. The alveolar space is the site of intense inflammatory and profibrotic reactions in the early phase of acute respiratory distress syndrome. Crit care med 1999; 27:304-312.
11. Yokokura H, Hiromatsu S, Akashi H, Kato S, and Aoyagi S. Effects of calsium channel blocker Azelnidipine on experimental abdominal aortic aneurysms. Surg Today 2007; 37:468-473.
12. Nakashima H, Aoki M, Miyake T, Kawasaki T, Iwai M et al. Inhibition of experimental aortic aneurysm in the rat by use of decoy oligodeoxynucleotides suppressing activity of nuclear factor κB and ets transcription factors. Circulation 2004; 109:132-138.
13. Fujiwara Y, Shiraya S, Miyake T, Yamakawa S, Aoki M et al. Inhibition of experimental abdominal aortic aneurysum in a rat model by the angiotensin receptor blocker valsartan. J Molecular Medicine 2008; 22:703.
14. Thompson RW, and Parks WC. Role of matrix metalloproteinase in abdominal aortic aneurysms. Ann NY Acad Sci 1996; 800:157-174.
15. Krupski WC. Arterial aneurysms. In: Rutherford RB, ed.Vascurar sugery. 4th ed Philadelphia: WB Saunders Company, 1995:1027-1028.
16. Tsunemi K, Takai S, Nishimoto M, Jin D, Sakaguchi M et al. Aspecifi chymase inhibitor, 2-(5-Formyamino-6-oxo-2-phenyl-1, 6-dihydropyrimidine-1-yl)-N-[{3, 4-dioxo-1-phenyl-7(2-pyridyloxy)}-2-hyptyl]acetamide (NK3201), suppresses development of abdominal aortic aneurysm in hamsters. J pharmacol Exp Ther 2004; 309:879-883.
17. Miyazaki M, Sakonjyo H, and Takai S. Anti-atherosclerotic effects of an angiotensin converting enzayme inhibitor and an angiotensin Ⅱ antagonist in cynomolgus monkeys fed a high-cholesterol diet. Br J Pharmacol 1999; 128:523-529.
18. Ihara M, Urata H, Kinoshita A, Suzumiya J, Sasaguri M et al. Increased chymase-dependent angiotensin Ⅱ formation atherosclerotic aorta. Hypertention1999; 33:1399-1405.
19. Nishimoto M, Takai S, Fukumoto H, Tsunemi K, Yuda A et al. Increased local angiotensin Ⅱ formation in aneurismal aorata. Life Science 2002; 71:2195-2205.
20. Thompson RW, and Baxter BT. MMP inhibition in abdominal aortic aneurysms. Rationale for a prospective randomized clinical trial. Ann N Y Acad Sci 1999; 878:159-178.
21. Jinno T, Iwai M, Li Z, Li JK, Liu HW et al. Calcium channel blocker Azelnidipine enhances vascular protective effect of AT1 receptor blocker olumesartan. Hypertension 2004; 43:263-269.
22. Rouet-Benzineb P, Gentro B, and Dreyfus P. Angiotensin Ⅱ induced nuclear factor-κ B activation in cultured neonatal rat cardiomyocytes through protein kinase C signaling pathway. J Mol Cell Cardiol 2000; 32:1767-1778.
23. Tsunemi K, Takai S, Nishimoto M, Yuda A, Sawada Y et al. Possible roles of angiotensin Ⅱ -forming enzymes, angiotensin converting enzyme and chymase-like enzyme, in the human aneurismal aorta. Hypertens Res 2002; 25:817-822.
24. Anidjar S, Dobrin PB, Chejfec G, and Michel JB. Experimental study of determinants of aneurismal expansion of the abdominal aorta. Ann Vasc Surg 1994; 8:127-136.
25. Halpern VJ, Nackman G, Gandhi RH, Irizarry E, Scholes JV et al. The elastase infunction of endogenous proteinase with matrix destruction and inflammatory cell response. J Vasc Surg 1994; 20:51-60.
26. Yajima N, Masuda M, Miyazaki M, Nakajima N, Chein S et al. Oxidatetive stress is involved in the development of experimental abdominal aortic aneurysm: a study of the transcription profile with complementary DNA microarray. J Vasc Surg 2002; 36:379-385.
27. Doris MT, Baby MM, Yi-Xin W, Dennis WW, Ronald V et al. Angiotensin Ⅱ is associated with activation of NF-κB-mediated genes and downregulation of PPARs. Physiol Genomics 2002; 11:21-30.
28. Reihardt D, Sigusch HH, Henβe J, Tyagi SC, Körfer R et al. Cardiac remodeling in and stage heart failure : upreguration of matrix metalloproteinase (MMP) irrespective of the underying disease, and evidence for a direct inhibitory effect of ACE inhibitors on MMP. Heart 2002; 88:525-530.
29. Zatina MA, Zarins CK, Gewertz BL, and Glagov S. Role of mediallamellar architecture in the pathogenesis of aortic aneurtsms. J Vasc Surg 1984; 1:442-448.

Original Contribution

Kurume Medical Journal, 57, 9-20, 2010

Analysis of Subendothelial Leukocyte Infiltration in the Trabecular Veins of Septic Spleen

OSAMU TAKASU*,**, TERUO SAKAMOTO**, MASAMICHI KOJIRO* AND HIROHISA YANO*

Departments of Pathology and Traumatology and Critical Care Medicine**, Kurume University School of Medicine, Kurume 830-0011, Japan*

Received 11 November 2009, accepted 27 January 2010

Edited by KOICHI OSHIMA

Summary: The splenic white pulp (WP) consists of CD20-positive lymph follicles (LFs) and CD3-positive periarteriolar lymphoid sheaths. Atrophy of the WP associated with a prolonged period of sepsis is a well-known pathological finding at autopsy. On the other hand, dense subendothelial leukocyte infiltration in the trabecular veins is also commonly observed in autopsy specimens of septic spleen. However, the characteristics and significance of this finding have not yet been well studied. In this study, autopsy spleens obtained from 55 sepsis and 45 non-sepsis patients were compared to determine the clinicopathological characteristics of subendothelial leukocyte infiltration in the trabecular veins, and its pathological significance was discussed. Severe and mild subendothelial leukocyte infiltration in the trabecular veins was observed in 45.5% of sepsis patients, but was absent in non-sepsis patients. Several clinicopathological characteristics of subendothelial leukocyte infiltration were identified. Firstly, the majority of infiltrated cells were lymphocytes. Secondly, both incidence and degree of infiltration were decreased at the late phase of sepsis accompanied by atrophy of the WP. Thirdly, types and compositions of infiltrated leukocytes reflected the histological findings of the spleen. Thus, the percentage of CD20-positive cells in the infiltrating cells into the subendothelium was proportional to the relative size of the CD20-positive area in the specimen, and the percentage of MUM1-p-positive cells in the infiltrating cells was proportional to the frequency of appearance of MUM1-p-positive cells in the red pulp. The CD20-positive area approximated the relative size of the WP in the septic cases, while the frequency of appearance of MUM1-p-positive cells was indicative of the differentiation levels of LFs into plasma cells upon antigen stimulation. Lastly, the intense subendothelial infiltration of CD20-positive cells was specific for the early stage of sepsis, and the morphological characteristics of these CD20-positive cells suggested their association with the marginal zone. Based on these clinicopathological characteristics and the fact that leukocyte infiltration into the subendothelium of trabecular veins became undetectable as atrophy of the WP progressed, it was suggested that the infiltrating cells had migrated from the WP, and this cell infiltration is an early activated immunological reaction in the spleen. Furthermore, the presence of possible efflux or drainage routes in the subendothelial spaces of trabecular veins was suggested.

Key words spleen, sepsis, trabecular vein, subendothelial leukocyte infiltration, lymphoid egress

INTRODUCTION

The spleen is the largest single mass of secondary lymphatic tissue in the human body, and the only lymphatic apparatus involved in the circulatory system. Two compartments, namely, the white pulp (WP)

Corresponding Author: Osamu Takasu, Department of Traumatology and Critical Care Medicine, Kurume University School of Medicine, 67 Asahi-machi, Kurume, 830-0011, Japan. Tel: +81-942-31-7732 Fax: +81-942-35-3920 E-mail: takasu_osamu@kurume-u.ac.jp

Abbreviations: LF, lymph follicle; MZ, marginal zone; PALS, periarteriolar lymphoid sheath; WP, white pulp.

containing mainly lymphoid cells, and the red pulp, containing non-lymphoid cells, are responsible for the immune function of the spleen. The former comprises T-lymphocyte-rich periarteriolar lymphoid sheaths (PALS) and B-lymphocyte-rich lymphoid follicles, which are surrounded by a marginal zone (MZ). The latter contains the vascular endothelium, a constituent of the splenic sinus, and histiocytes. Histopathological changes of these compartments caused by pathogens in the blood and humoral mediators, such as inflammatory cytokines and lipopolysaccharides, were shown by experimental studies [1-7]. It is also well-known that different intensities of atrophy and swelling of the WP occur in patients with severe sepsis, depending on the types of pathogens and length of illness, and that neutrophils and histiocytes appear in the red pulp [8,9].

On the other hand, subendothelial leukocyte infiltration in the trabecular veins is considered to be an empirical finding characteristic of human autopsy specimens of a septic spleen. However, this characteristic cell infiltration has not yet been studied in detail in experimental models or human spleen specimens, so its pathological characteristics and significance are unclear. In this study, we obtained autopsy specimens from patients with sepsis and performed immunostaining of the major immunocompetent cells in the spleen, namely, B- and T-lymphocytes, plasma cells, histiocytes and neutrophils. We aimed to clarify 1) the characteristics of subendothelial leukocyte infiltration in the trabecular veins, and 2) the relationships between histological changes in the spleen and leukocyte infiltration into the subendothelium of trabecular veins, and we discuss the pathological significance of our findings.

MATERIALS AND METHODS

Tissue samples

Spleens from 100 individuals were selected from consecutive autopsy cases at Kurume University Hospital between 1984 and 2004. All selected cases had received intensive treatment for critical conditions at the Emergency and Critical Care Center. The 100 spleens consisted of 55 sepsis cases and 45 non-sepsis cases as controls. The 55 sepsis cases consisted of 24 cases of peritonitis, 22 cases of critical pneumonia and 9 cases of pyelonephritis (urosepsis) or soft-tissue infections. The controls consisted of 21 cases of acute myocardial infarction, 14 cases of ruptured aortic aneurysm/acute aortic dissection, 5 thromboembolisms of the pulmonary artery and 5 cases of cerebrovascular disease. The absence of infectious complications in the controls was confirmed at autopsy. The following cases were excluded from this study: those whose clinical period was unknown, those with cirrhosis, chronic heart failure or long-term treatment with steroids or immunosuppressants, and those whose splenic samples showed either abscess, hematoma or episplenitis.

Sepsis criteria

We applied the sepsis criteria of Hotchkiss et al. [9] In short, a case was clinically diagnosed as sepsis when the patient had altered mental status, hemodynamic instability requiring vasopressors, and hypo- or hyper-thermia; and in addition, the case satisfied one of the following: (i) bacteria, fungi or endotoxin was positive in blood, abdominal fluid or tissue culture, (ii) infection was remarkable at surgical observation (e.g., perforated large bowel with peritoneal contamination), or (iii) a histopathologic diagnosis of infection at postmortem examination (e.g., bronchopneumonia and intra-abdominal abscess).

Morphological observation and evaluation

On HE-stained specimens, the presence/absence of infiltrating leukocytes in the subendothelial space of the trabecular veins and its degree were evaluated according to the following three grades (Fig. 1): (i) Severe infiltration: subendothelial leukocyte infiltration was observed in almost all trabecular veins and more than half of the veins presented infiltration in several or more layers; (ii) Mild infiltration: subendothelial leukocyte infiltration was observed in almost all the trabecular veins, but the infiltration was not continuous or consisted primarily of a single layer; (iii) No infiltration: there was no subendothelial leukocyte infiltration except in sporadic cells. Each specimen was examined by experienced pathologists (OT, MK) who were unaware of the cause of death or other clinical information.

Immunohistochemistry

Immunohistochemistry was performed to determine the type of infiltrating leukocytes in the subendothelial spaces of the trabecular veins and for morphometric quantification of the WP and the red pulp.

Formalin-fixed, paraffin-embedded blocks of splenic tissue were re-cut and subjected to immunohistochemistry. The primary antibodies used in this study are summarized in Table 1. Each specimen was cut into 4-μm-thick slices on numbered glasses, pretreated for epitope retrieval of (i) anti-CD20 and anti-

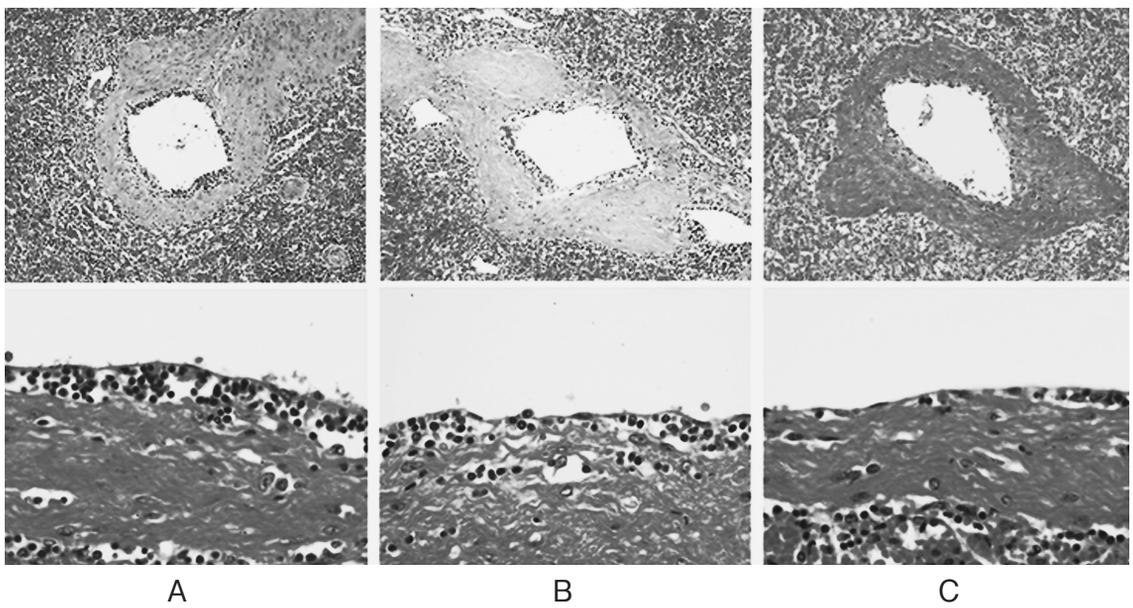

Fig. 1. Grade of leukocyte infiltration in the subendothelial space.
A) Severe infiltration: leukocytes infiltrated several or more layers. B) Mild infiltration: leukocytes infiltrated a few layers. C) No infiltration: There was no infiltration except for sporadic cells (HE stain, upper columns ×100. Lower columns ×400).

TABLE 1.
Antibodies used in the study and their sources and specificities

Antibody	Antigen/Clone	Working dilution	Specificity
Anti-LCA*	CD45, Leukocyte common antigen / L26	1 : 1	Lymphoid cells without plasma cells
Anti-CD20**	CD20cy/ L26	1 : 1	B cells in all compartments
Anti-CD3**	CD3	1 : 1	T cells in all compartments
Anti-MUM1 protein**	/ MUM1p	1 : 50	Late stages of B-cell differentiation, Plasma cells
Anti-CD68**	/ PG-M1	1 : 100	Red pulp cordal and intrasinusoidal macrophages, germinal center tangible body macrophages
Anti-myelo-peroxidase***	Myeloperoxidase /59A5	1 : 150	Neutrophil granulocytes, monocytes and precursors of granulocyte

* Thermo Electron Corp. (Pittsburgh, USA),
** Dako Cytomation (Carpinteria, USA),
*** Novocastra Laboratories Ltd. (Newcastle, UK)

MUM1 protein [10] with 10-min microwave treatment at 100°C using 0.01 mol/L citrate buffer, pH 6.0; (ii) anti-CD3 with 10-min microwave treatment at 100°C using 1 mmol/L EDTA, pH 8.0; and (iii) anti-CD68 (PG-M1) with 0.1% trypsin treatment for 30 min at 37°C. Immunohistochemistry was performed using HISTOFINE SAB-PO kits (Nichirei Biosciences Inc., Tokyo, Japan) with an established streptavidin-biotin complex immunoperoxidase method and 3'3'-diaminobenzidine (DAB) as substrate.

Type of infiltrating leukocytes

Infiltrating leukocytes in the subendothelial space of the trabecular veins were analyzed on each immu-

nohistochemical specimen, which were stained with anti-CD20 antibody, anti-CD3 antibody, anti-MUM1-p antibody, anti-CD68 antibody or anti-myeloperoxidase antibody. The number of positive and non-positive cells to each antibody was counted in predetermined veins among the sequential specimens until the cell counts became at least 1000. The positive rate was calculated in each specimen, and each positive rate was assessed for SI-CD20 (%), SI-CD3 (%), SI-MUM1-p (%), SI-CD68 (%) and SI-Myelo (%).

Other histological parameters and clinical information

Three additional histological parameters-percentage area of the WP and percentage area of lymph follicles (LFs) to the total area of the specimen, and the number of anti-MUM1 protein-positive cells in the red pulp-were calculated for each immunohistochemical specimen as detailed below.

Patient age, primary disease and clinical period (days) were obtained from clinical charts, and spleen weight (g) was obtained from the autopsy record.

The obtained data were comparatively analyzed for the relationship between histological parameters and clinical information.

Calculation of percentage area of WP/LFs to the total area of the specimen

Three independent areas on each immunohistochemical specimen that was stained with anti-LCA or anti-CD20 antibody were photographed using an AX80 microscope (Olympus, Tokyo, Japan) and a digital camera DP70 (Olympus, Tokyo, Japan, magnification, ×12.5). To avoid underestimation, the subcapsular areas, which consist predominantly of the red pulp, were excluded from the sampling [11]. From the digital data, the percentage of LCA or CD20-positive area to the total area was obtained using image analysis software, MacSCOPE version 2.58 (Mitani Corporation, Tokyo, Japan); the average of the three shots was calculated and shown as %LCA or %CD20, respectively.

Count of anti-MUM1-p antibody positive cells in the red pulp

Immunohistochemical specimens stained with anti-MUM1-p antibody were examined under an optical microscope CX41 (Olympus, Tokyo, Japan) equipped with a cross-section eyepiece micrometer U-OCM-SQ10/10 (Olympus, Tokyo, Japan) at a high-power field (magnification, ×400). The number of positive cells that showed strong MUM1-p nuclear positivity in addition to weaker labeling of the cytoplasm [10] was counted in a 250×250 μm area of the red pulp that did not contain trabeculae or penicillus. Counting was performed in five independent areas in each specimen, and the average was shown for RP-MUM1-p.

Statistical analysis

The obtained data were expressed as mean ± SD. For the histological parameters, between-group analysis was performed using Student's *t* test or Welch's *t* test. The Steel-Dwass test was used for multiple comparisons among the groups of sepsis, and Steel's test was used to compare the subgroups of sepsis with the control group. Pearson's correlation analysis was used to estimate the correlation. These statistical analyses

TABLE 2.
Clinical and histological features according to the degree of infiltration

	Control (n : 45)	Degree of leukocyte infiltration in sepsis cases		
		Severe (n : 12)	Mild (n : 13)	No infiltration (n : 30)
Age (years old)	66±13	61±16	60±15	65±15
Disease period (days)	3.0±1.9	8.8±5.6 [a,b,c]	17.2±8.2 [a,d]	24.5±13.9 [a,d]
Spleen weight (g)	99±42	117±66	167±87	171±99 [a]
%LCA (%)	15.1±4.8	10.2±4.3 [a,b]	6.5±1.8 [a]	5.6± 2.8 [a,d]
%CD20 (%)	12.7±4.3	8.7±3.6 [a,b]	5.0±2.2 [a]	4.4±2.7 [a,d]
RP-MUM1-p	26±13	45±22 [a]	76±46 [a]	72±49 [a]

%LCA: percentage of LCA-positive area to the total area. %CD20: percentage of CD20-positive area to the total area. RP-MUM1-p: the number of MUM1-p positive cells in red-pulp.
a: $P<0.05$, vs. controls. b: $P<0.05$, vs. no infiltration group. c: $P<0.05$, vs. mild infiltration group. d: $P<0.05$, vs. severe infiltration group.

were performed using Microsoft Excel (R) 2007 with the add-in software Ekuseru-Toukei 2008 (Social Survey Research Information Co., Ltd., Japan). Values of *P* less than 0.05 were considered significant.

RESULTS

Positive rate and grade of subendothelial leukocyte infiltration

Subendothelial leukocyte infiltration was found in 25 of the 55 sepsis cases (45.5%). Of these, 12 had severe infiltration and 13 had mild infiltration. In contrast, there were no severe or mild infiltration cases in the controls. As the 25 positive cases consisted of 11 cases of peritonitis, 9 cases of pneumonia and 5 cases of others, there was no disease specificity.

Clinical and pathological (histological) characteristics in positive cases

The clinical and pathological (histological) characteristics in the two sepsis groups with or without subendothelial leukocyte infiltration were as follows: age: 60.1±14.9 vs. 65.4±14.7; clinical periods (day): 13.2±8.2 vs. 24.5±13.9; spleen weight (g): 142.8±80.2 vs. 170.6±99.2; %LCA (%): 8.3±3.7 vs. 5.6±2.8; %CD20 (%): 6.8±3.4 vs. 4.4±2.7; and RP-MUM1-p: 61.3±40.7 vs. 71.7±49.3. Clinical periods, %LCA and %CD20 were significantly different between these two groups.

Table 2 shows a summary of these clinical and pathological characteristics according to the grade of subendothelial leukocyte infiltration in sepsis cases and controls. In the sepsis cases, the clinical period of severe infiltration cases was significantly shorter than in both the non-infiltration and mild infiltration cases. Although significant differences in spleen weight were not observed among the three degree-groups of sepsis, the weight of the non-infiltrating cases was higher than that of the controls.

For histological parameters, both %LCA and %CD20 were smaller in every grade of sepsis than those in the controls. In contrast, RP-MUM1-p was higher in every grade of sepsis than that in the controls. Among the three grades of sepsis, both %LCA and %CD20 in severe infiltration cases were significantly higher than those in non-infiltration cases.

Relationship between subendothelial leukocyte infiltration and clinical periods

Clinical periods in sepsis cases were divided into three categories: 7 days or shorter, 8-28 days, and 29 days or longer. The case number in every grade of subendothelial infiltration is shown in Fig. 2. Cases of 7 days or shorter presented an apparently high positive rate (61.5%) of subendothelial leukocyte infiltration. However, the positive ratio decreased as the clinical period lengthened. The ratio of severe infiltrating cases was high in cases of 7 days or shorter. However, no severe infiltration cases and only one mild infiltration case was observed when the clinical period was 29 days or longer.

Type and ratio of infiltrating cells

Various cells such as small or medium-sized lymphocytes, monocytes, plasma cells and granulocytes were observed in the subendothelial space in HE-stained specimens. Most of these cells were stained by either anti-CD20, anti-CD3, anti-MUM1-protein, anti-CD68 or anti-myeloperoxidase antibody. In all 25 cases with subendothelial leukocyte infiltration, the total of SI-CD20 (%), SI-CD3 (%), SI-MUM1-p (%), SI-CD68 (%) and SI-Myelo (%) was 90% or higher (average: 95.3±3.5%). The total of SI-CD20 (%), SI-CD3 (%) and SI-MUM1-p (%) in each case occupied the majority of the total value, ranging from 69.2 to 94.3% (average: 81.5±6.5%).

Figure 3 shows the rate of each infiltrating cell type in the subendothelial infiltration of 25 positive cases. Comparing cases of 7 days or shorter with those of 8 days or longer, the SI-CD3 (%) in both categories were relatively high without any significant differences. On the other hand, the SI-CD20 (%) in cases 7

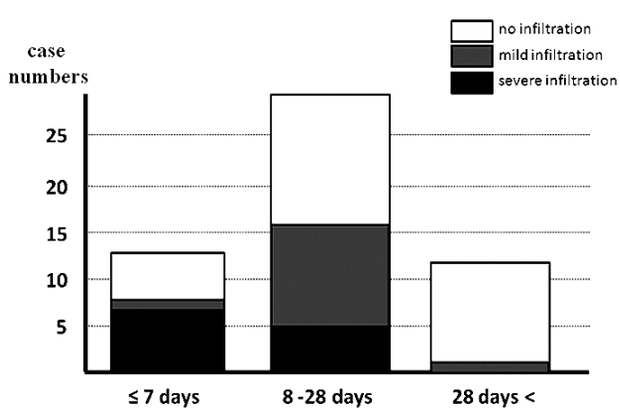

Fig. 2. Case number and grade of subendothelial infiltration in three categories of clinical periods.
Along with the prolongation of clinical periods, the positive cases of subendothelial leukocyte infiltration and the ratio of severe infiltration cases (black bar) tended to decrease.

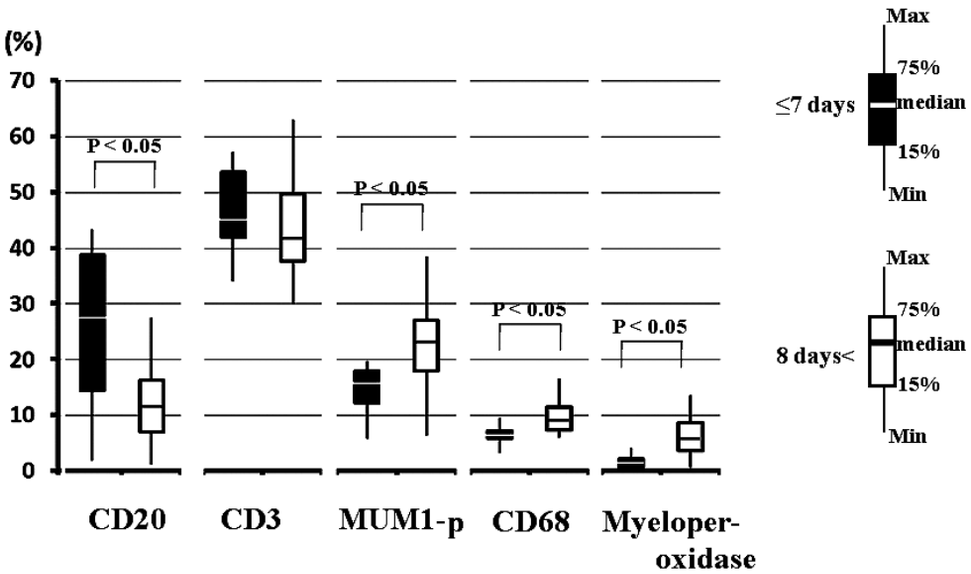

Fig. 3. Differences in infiltrating cell types according to the clinical periods.
The ratio of CD3-positive cells was relatively high in both periods. A high SI-CD20 (%) rate is a characteristic finding in the early phase of sepsis. In contrast, SI-MUM1-p (%), SI-CD68 (%) and SI-Myelo (%) rates in the cases of 8 days or longer were significantly higher than those in the cases of 7 days or shorter.

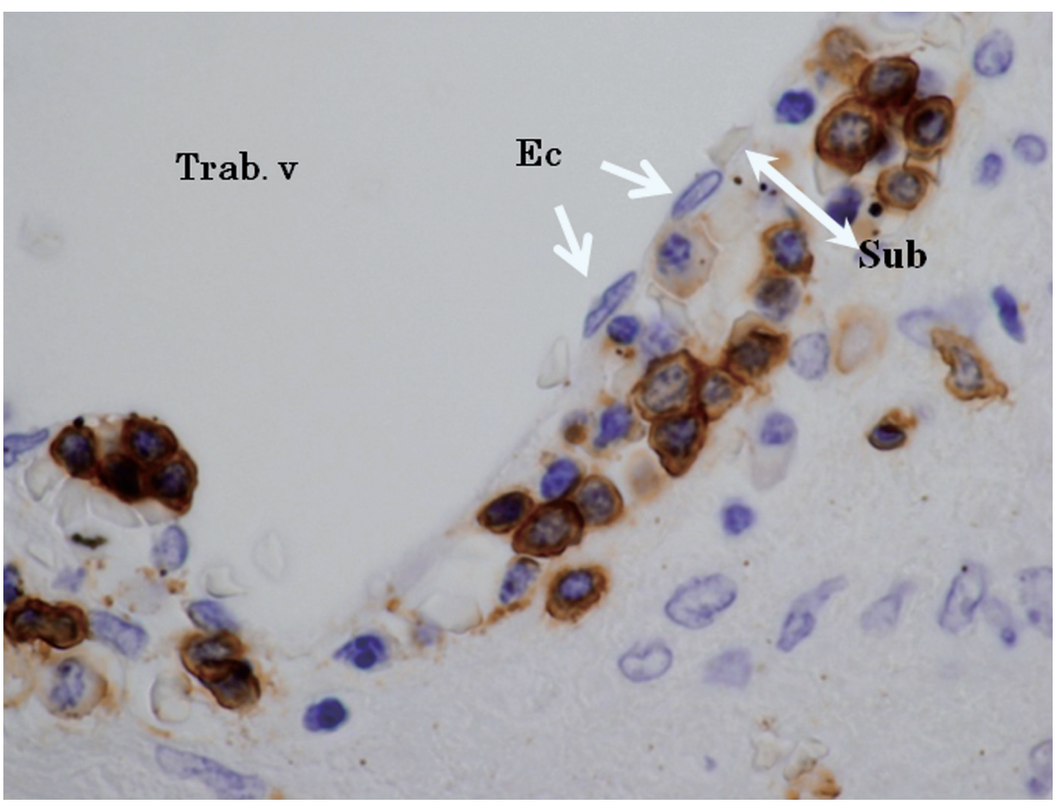

Fig. 4. Morphological characteristics of CD20-positive cells in subendothelial spaces.
Various cells, such as small or medium-sized lymphocytes and plasma cells, infiltrated the subendothelial spaces of the trabecular vein in the septic spleen. CD20-positive cells showed distinct morphological characteristics, such as intermediate-sized lymphocytes with a relatively abundant cytoplasm (Brown: anti-CD20 Ab positive B cells, Trab. V: trabecular vein, Ec: endothelial cell, Sub: subendothelial space).

days or shorter was higher than that in those 8 days or longer. In contrast, SI-MUM1-p (%), SI-CD68 (%) and SI-Myelo (%) were significantly higher in the cases 8 days or longer than in those of 7 days or shorter.

Morphological characteristics of CD20-positive cells in subendothelial spaces

The infiltrating CD20-positive lymphocytes in subendothelial spaces showed distinct morphological characteristics such as intermediate-sized lymphocytes with relatively abundant cytoplasm (Fig. 4).

Relationship between the histological parameters and the relationship between the histological parameters and subendothelial leukocyte infiltration

Results of the histological parameter analysis are shown in Fig. 5, and a schema based on the results is shown in Fig. 6. As shown in Fig. 5, a significant positive relationship was observed between %CD20 and SI-CD20 (%) (r=0.69, $P<0.01$, Fig. 5A), and between RP-MUM1-p and SI-MUM1-p (%) (r=0.62, $P<0.01$, Fig. 5B). This implies that the percentage of CD20-positive B-lymphocytes in the cells infiltrating into the subendothelium of trabecular veins (SI-CD20 (%)) was high in cases with mild atrophy of LFs contained in the MZ (a small decrease in %CD20) (Fig. 6B), while the percentage of CD20-positive cells in the subendothelium was low in cases with severe atrophy of LFs (Fig. 6C). Also, the percentage of MUM1-p-positive cells in the cells infiltrating into the subendothelium increased as the number of MUM1-p in the

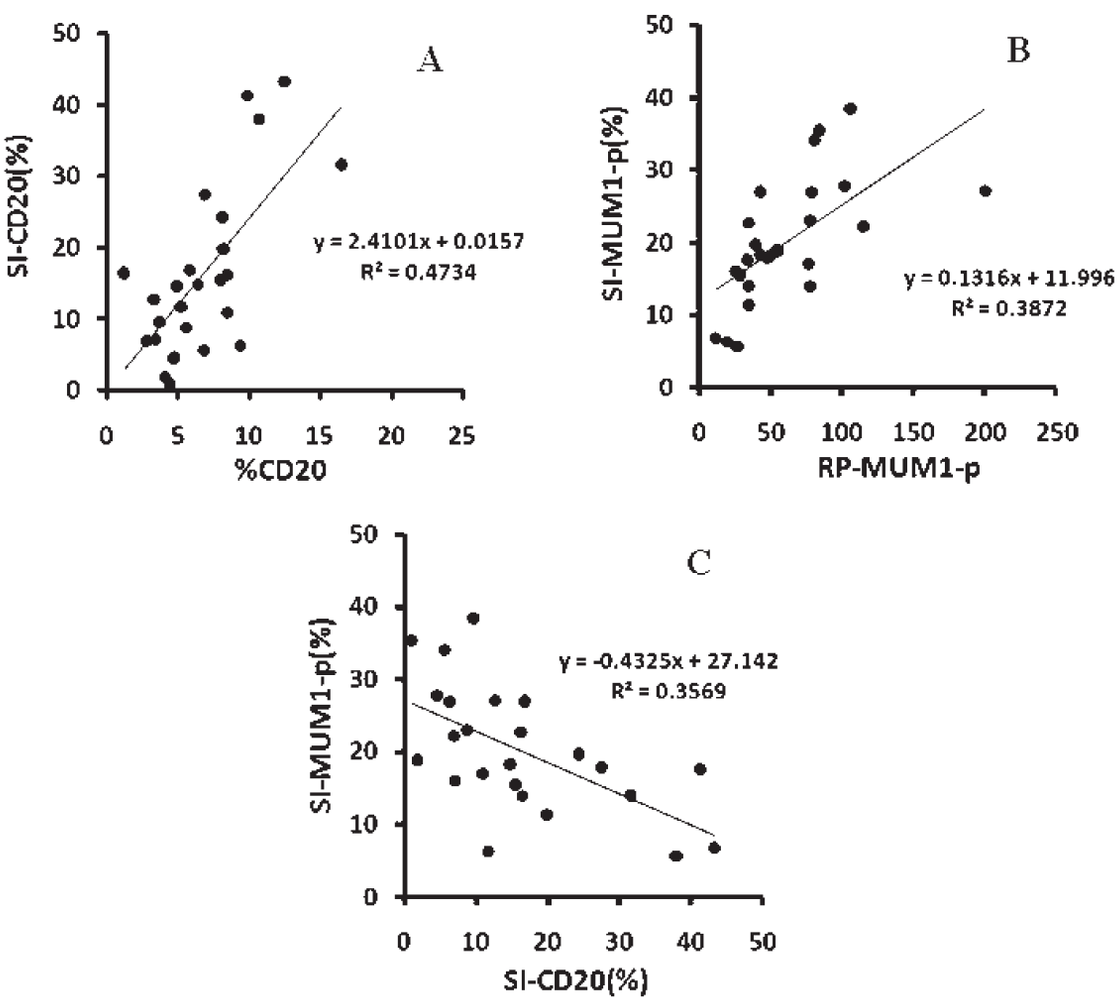

Fig. 5. Relationship between histological parameters and the rate of infiltrating cells.
A) Positive relationship between %CD20 and SI-CD20 (%) (r=0.69). B) Positive relationship between RP-MUM1-p and SI-MUM1-p (%) (r=0.63). C) Negative relationship between SI-CD20 (%) and SI-MUM1-p (%) (r=0.60).

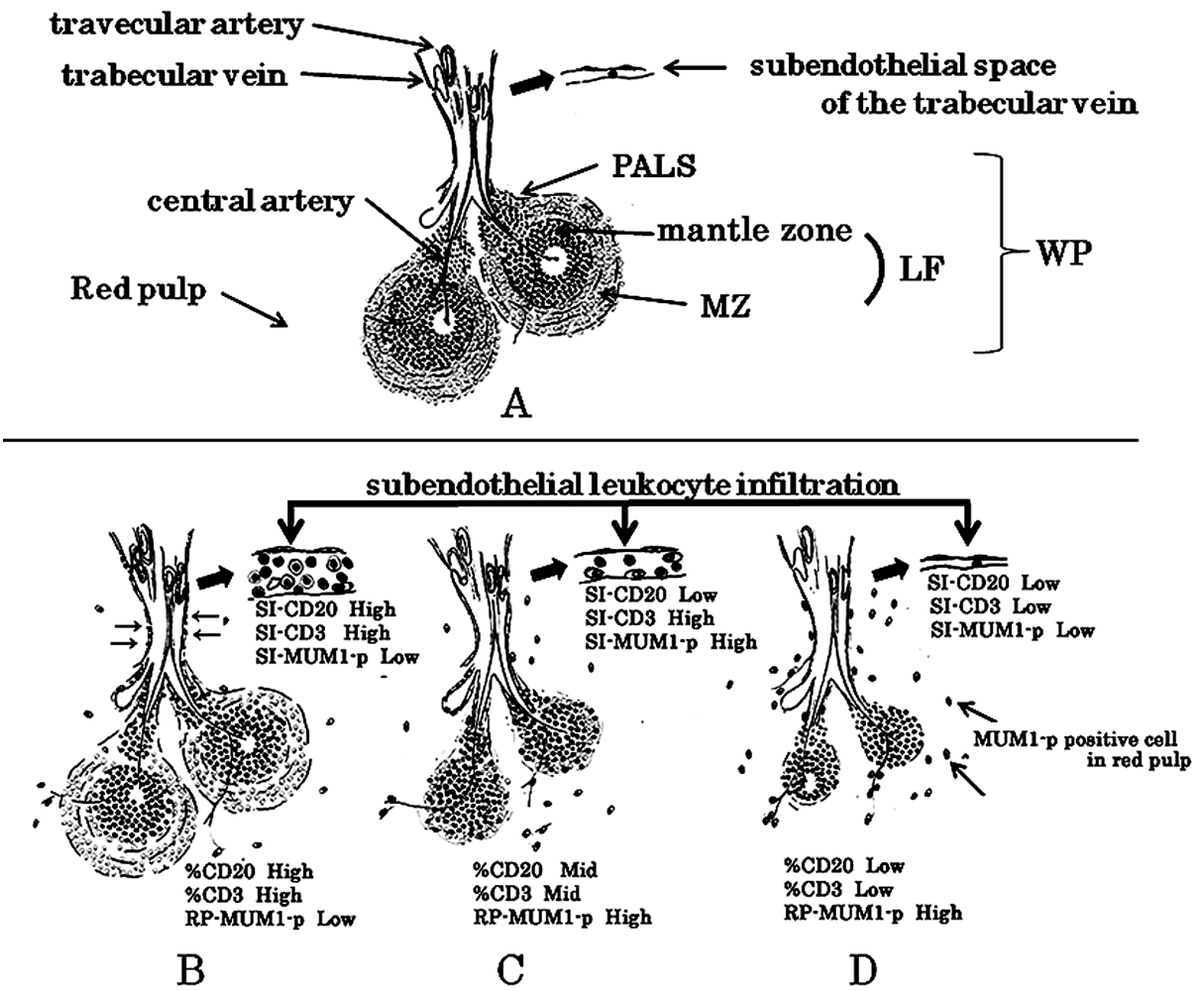

Fig. 6. A scheme depicting the results of histologic parameter analysis.

A) Non-sepsis (control) case. The WP was well defined without a sign of atrophy. The MZ was well defined at the most outer layer in LFs. There were hardly any MUM1-p-positive cells in the red pulp. There was hardly any cell infiltration in the subendothelial spaces of trabecular veins. LF, lymph follicle; MZ, marginal zone; PALS, periarteriolar lymphoid sheath; WP, white pulp.

B) Septic case accompanied by mild atrophy of the WP. In LFs, the number of cells in both the MZ and mantle zone decreased. The MZ was defined but slightly unclear. The PALS region became void as the cell number decreased. Many CD20- and CD3-positive cells were found in the subendothelial spaces of trabecular veins and peritrabecular spaces (arrows).

C) Septic case accompanied by moderate atrophy of the WP. Atrophy was more severe than that observed in B. Many MUM1-p-positive cells with the nucleus containing slightly uneven distribution of cartwheel-like chromatins were present in the red pulp. Cells in the subendothelial spaces of trabecular veins were mainly composed of CD3-positive lymphocytes and MUM1-p-positive cells, while the CD20-positive cell population was small. The extent of cell infiltration was slightly less than that observed in B; however, the percentage of infiltrating CD3-positive cells (SI-CD3%) was not significantly different from that observed in 6B.

D) Septic case accompanied by severe atrophy of the WP. Severe atrophy was observed in both LF and PALS regions. The MZ was obscure. Only sporadic cell infiltration was observed in the subendothelial spaces of trabecular veins. Many MUM1-p-positive cells were present in the red pulp.

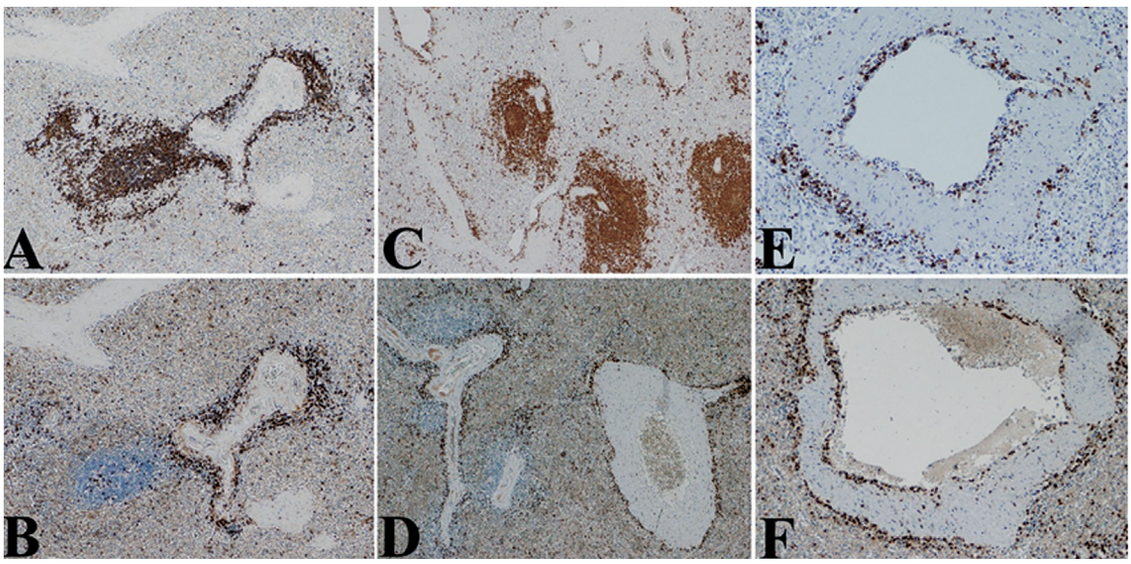

Fig. 7. Immunohistochemical distribution of leukocytes in sepsis cases.
A) CD20-positive lymphocytes in a mild white pulp depletion case (×40). Lymphocyte depletion was marked in the inner part of the marginal zone (MZ). CD20-positive lymphocytes were observed in the periarterial lymphatic sheath (PALS) and the peritrabecular space. B) CD3-positive lymphocytes in the same case and the same area as shown in Fig. A (×40). The number of CD3-positive lymphocytes was decreased in the PALS, and these cells were present in the peritrabecular space that coincided with the CD20-positive area as shown in Fig. A. C) CD20-positive lymphocytes infiltrated the peritrabecular space (×40). D) CD3-positive lymphocytes infiltrated around the thick trabeculae (×40). E, F) Lymphocyte infiltration with a double-ring-like appearance due to infiltration to both the subendothelial space and the peritrabecular space (×100) (A, C, E: immunostaining for CD20; B, D, F: immunostaining for CD3).

red pulp (RP-MUM1-p) increased (Fig. 6B and 6C). There was a negative correlation between SI-CD20 (%) and the SI-MUM1-p (%) ($r=-0.60$, $P<0.01$, Fig. 5C).

Characteristic distribution of lymphocytes in sepsis cases

Characteristic distributions of the lymphocytes in sepsis cases were observed in comparison to the controls. (i) Remarkable cell depletion was observed in both the MZ and the PALS of the WP. Even in the cases with mild WP atrophy, the number of CD20-positive lymphocytes of the inner MZ was obviously decreased (Fig. 7A, cf. Fig. 6B). On the other hand, the number of CD3-positive lymphocytes was decreased in the PALS, and a relatively high number of CD20-positive lymphocytes was found in this area (Fig.7B). (ii) CD20- and CD3-positive lymphocytes were distributed not only in the PALS but also in the peritrabecular area attached to the WP (Fig. 7A, 7B). Lymphocytes were also observed around thick trabeculae (Fig. 7C, 7D, cf. arrow head in Fig. 6B). (iii) Some cross sections of the trabecular vein presented a double-ring like-appearance due to lymphocytes in both the subendothelial space and the peritrabecular space (Fig. 7E, 7F). These findings were typical in the severe infiltrating cases.

DISCUSSION

Subendothelial leukocyte infiltration in the trabecular veins was a characteristic histological finding in cases of septic spleen compared with non-sepsis cases. This histological finding was especially typical in the acute phase of sepsis.

One of the conspicuous histological differences between sepsis cases with and without subendothelial leukocyte infiltration was the degree of atrophy in the WP (LFs including the MZ and PALS). With regard to WP atrophy in a septic human spleen, Hotchkiss et al. [9] reported that that caspace-9-mediated lymphocyte apoptosis induced progressive profound depletion of B and $CD4^+$-T lymphocytes, and lymphoid depletion occurs in sepsis cases with a long clinical course. We also found marked atrophy in LFs in the B-lymphocyte zone and the $CD4^+$ T-lymphocyte-rich PALS zone in patients with prolonged illness of 29 days or longer and with low intensity of cell infiltration in the trabec-

ular vein subendothelium. These results suggest a potential link between atrophy of the WP and depletion of subendothelial cell infiltration in the trabecular veins.

To summarize the pathological characteristics in positive cases of subendothelial infiltration, i) the infiltrating leukocytes were mainly lymphocytes, ii) both the positive rate and the degree of infiltration were decreased in the late phase of sepsis along with WP atrophy (Fig. 6C), iii) types and compositions of infiltrated leukocytes correlate to histological parameters, such as %CD20 and RP-MUM1-p (Fig. 6B, 6C), iv) a high ratio of CD20-positive lymphocytes in infiltrating cells was a characteristic finding that was limited to the early phase of sepsis (Fig. 6B). These CD20-positive lymphocytes were correlated with the MZ based on the morphological characteristics of infiltrating cells. In specimens of patients with sepsis, the boundary between the small-sized B lymphocyte-rich mantle zone and the surrounding MZ was unclear in LFs, and CD20-positive lymphocytes spread into the PALS region, thus the percentage of the CD20-positive area (%CD20) was approximate to the area percentage of the WP. Upon antigen presentation, plasma cells migrate from LFs via the PALS region and along the terminal arterioles into the red pulp [7]. Taken together, both %CD20 and the number of MUM1-p positive cells (post-germinal B lymphocytes and plasma cells) in the red pulp are considered to indicate the levels of WP activation. A significant correlation between these histological findings (%CD20 and PR-MUM-1-p) and the percentage of CD20-positive cells and MUM1-p-positive cells in the subendothelial spaces of trabecular veins suggests that evidence of subendothelial cell infiltration in trabecular veins also reflects the status of immunological activation in the spleen [12].

Based on these clinicopathologic characteristics, subendothelial leukocyte infiltration in the trabecular veins may reflect the migration of cells from the WP. Similar manifestations were found in the non-septic spleen of cancer or tumor patients [13-16] and in the transplanted liver and kidney of patients with transplant vasculitis [17]. However, the infiltrating cells in the former cases were tumor cells such as leukemia and cancer cells, and those in the latter cases were mainly T-lymphocytes [17], thus their histopathological characteristics are different from those found in this study. Moreover, taking the decrease and disappearance of the infiltrating cells from the subendothelial spaces in the late phase of sepsis into consideration (Fig. 6D), the existence of efferent or drainage routes was suspected in the subendothelial spaces of the trabecular vein.

For the lymphocytes that leave the WP, there are two possible routes of exit, namely, via the blood or via the efferent lymph [18]. Via the blood, in the rodent spleen, 'marginal zone bridging channels' [19] or 'lymphocyte sheaths around the terminal arterioles' [20] have been described as passageways for lymphocytes from the MZ into the red pulp. Many of the MUM1-p-positive cells in the red pulp were found around the terminal arterioles, suggesting trafficking of these cells via this route. However, since efferent lymphatics are not as apparent in the spleen as in other peripheral lymphatic tissue, the exact anatomical route is not known in detail. Furthermore, the involvement of lymphatics in the transport of lymphocytes from the WP and the precise molecular mechanisms have not yet been elucidated [21].

However, a large lymph plexus surrounding the central artery and periarterial lymphatics in the trabeculae of the spleen have been clearly demonstrated in both the rodent [22-25] and the human [26-29]. As lymphoid depletion in the PALS similar to that in sepsis cases has been demonstrated in prolonged drainage of the thoracic duct [30,31], lymphoid depletion in the PALS could also account for the efflux of lymphocytes as a non-apoptotic mechanism.

In contrast to the periarterial lymphatics, the presence of subintimal lymphatic spaces under the venous endothelium has been demonstrated only in the human spleen [15,16,29]. Fukuda [29] reported perivenous lymphatics in addition to periarterial lymphatics as efferent lymphatics in autopsy specimens of the normal human spleen. By means of serial sections, he showed that perivenous lymphatics were found to be a continuity of Billroth's cords, where they were accompanied by venous sinuses at their entrance into the trabeculae. These subintimal spaces, which were initially found to be slit-shaped, became definite vessels that had distinct endothelial linings on their way to the hilus [29], and were consistent with the subendothelial space that was observed during dense leukocyte infiltration in sepsis cases. Moreover, the present study shows that the slit-shaped subendothelial space is contiguous to the peritrabecular space. As this space is contiguous to the PALS and MZ, this continuous route is presumed to be the major inflow to the subendothelial space from the WP.

The high infiltration of CD20-positive lymphocytes with a relatively abundant cytoplasm such as MZ B cells was a characteristic feature that was limited in the early phase of sepsis. It is well known that reacti-

vated B cells upon administration of lipopolysaccharides or IL-1 migrate from the MZ into the inner region of LFs and the PALS in experimental rodent models [1-6], while migration of B cells in the MZ to the subendothelial spaces of trabecular veins has not yet been reported. Interestingly, whereas MZ B cells of rodents are restricted to the spleen and do not recirculate [32-35], human splenic MZ B cells are reported to recirculate [36,37]. It is possible that the intermediate-sized CD20-positive lymphocytes in subendothelial spaces are identical to the recirculating MZ B cells, but additional studies are needed to confirm this hypothesis.

Based on our analysis, it may be presumed that the subendothelial leukocyte infiltration reflects cell migration from the WP (or the lymph stasis [16]) as an early activated immunologic reaction. Moreover, the presence of an efferent or drainage route is presumed in the subendothelial space of trabecular veins. Immunostaining using anti-lymphoepithelial antibody (D2-40) demonstrated perivenous lymphatics in the subendothelial space of the trabecular vein, together with periarterial lymphatics (data not shown). To demonstrate the egress of lymphocytes via perivenous lymphatics in the human spleen in sepsis, further studies are needed to assess the mechanism of lymphocyte egress from the spleen or to identify an adhesion molecule and ligand on lymphatics and lymphocytes.

REFERENCES

1. Cinamon G, Matloubian M, Lesneski MJ, Xu Y, Low C et al. Sphingosine 1-phosphate receptor 1 promotes B cell localization in the splenic marginal zone. Nat Immunol 2004; 5:713-720.
2. Lopes-Carvalho T, and Kearney JF. Development and selection of marginal zone B cells. Immunol Rev 2004; 197:192-205.
3. Groeneveld PH, Erich T, and Kraal G. In vivo effects of LPS on B lymphocyte subpopulations. Migration of marginal zone-lymphocytes and IgD-blast formation in the mouse spleen. Immunobiology 1985; 170:402-411.
4. Groeneveld PH, and van Rooijen N. In vivo effects of lipopolysaccharide on lymphoid and non-lymphoid cells in the mouse spleen. Reduction of T-lymphocytes and phagocytosis in the inner parts of the periarteriolar lymphocyte sheath. Cell Tissue Res 1984; 236:637-642.
5. Vinuesa CG, Sunners Y, Pongracz J, Ball J, Toellner KM et al. Tracking the response of Xid B cells in vivo: TI-2 antigen induces migration and proliferation but Btk is essential for terminal differentiation. Eur J Immunol 2001; 31:1340-1350.
6. Attanavanich K, and Kearney JF. Marginal zone, but not follicular B cells, are potent activators of naive CD4 T cells. J Immunol 2004; 172:803-811.
7. Eikelenboom P, Boorsma DM, and van Rooijen N. The development of IgM- and IgG-containing plasmablasts in the white pulp of the spleen after stimulation with a thymus-independent antigen (LPS) and a thymus-dependent antigen (SRBC). Cell Tiss Res 1982; 226:83-95.
8. Gunia S, Albrecht K, May M, and Stosiek P. The white pulp in the setting of the septic spleen caused by different bacteria: a comparative morphometric study. APMIS 2005; 113:675-682.
9. Hotchkiss RS, Tinsley KW, Swanson PE, Schmieg RE Jr, Hui JJ et al. Sepsis-induced apoptosis causes progressive profound depletion of B and $CD4^+$ T lymphocytes in humans. J Immunol 2001; 166:6952-6963.
10. Falini B, Fizzotti M, Pucciarini A, Bigerna B, Marafioti T et al. A monoclonal antibody (MUM1p) detects expression of the MUM1/IRF4 protein in a subset of germinal center B cells, plasma cells, and activated T cells. Blood 2000; 15:2084-2092.
11. van Krieken JH, te Velde J, Hermans J, Cornelisse CJ, Welvaart C et al. The amount of white pulp in the spleen; a morphometrical study done in methacrylate- embedded splenectomy specimens. Histopathology 1983; 7:767-782.
12. Neiman RS, Orazi A. Spleen. Anderson's Pathology. 10th ed. Edited by Damjanov I, Linder J. St. Louis, Mosby-Year Book, Inc., pp1201-1217, 1996.
13. Burke JS, Sheibani K, Winberg CD, and Rappaport H. Recognition of hairy cell leukemia in a spleen of normal weight. The contribution of immunohistologic studies. Am J Clin Pathol 1987; 87:276-281.
14. Edelman M, Evans L, Zee S, Gnass R, and Ratech H. Splenic micro-anatomical localization of small lymphocytic lymphoma/chronic lymphocytic leukemia using a novel combined silver nitrate and immunoperoxidase technique. Am J Surg Pathol 1997; 21:445-452.
15. Goldberg GM. Lymphatics of the spleen. J Anat 1958; 92:310-314.
16. Goldberg GM. A study of malignant lymphomas and leukemias. VI. Lymph stasis versus lymphogenous leukemia of the spleen. Cancer 1962; 15:882-889.
17. Feingold RE, and Churg J. Transplant vasculitis. In: Churg A, Churg J, editors. Systemic vasculitides. New York, Igaku-Shoin, pp351-7, 1991.
18. Brozman M. Anatomical pathways from the white to the red pulp in the human spleen. Acta Anat 1985; 121:189-193.
19. Mitchell J. Lymphocyte circulation in the spleen. Marginal zone bridging channels and their possible role in cell traffic. Immunology 1973; 24:93-107.
20. van Rooijen N, Claassen E, and Eikelenboom P. Is there a single differentiation pathway for all antibody-forming cells in the spleen? Immunol Today 1986; 7&8:193-196.
21. Mebius RE, and Kraal G. Structure and function of the spleen. Nat Rev Immunol 2005; 5:606-616.
22. Pellas TC, and Weiss L. Deep splenic lymphatic vessels in the mouse: a route of splenic exit for recirculating lymphocytes. Am J Anat 1990; 187:347-354.
23. Janout V, and Weiss L. Deep splenic lymphatics in the marmot: an electron microscopic study. Anat Rec 1972; 172:197-219.
24. Hokazono K, and Miyoshi M. Scanning- and transmission

electron-microscopic study of lymphatic vessels in the splenic white pulp of the macaque monkey. Cell Tissue Res 1984; 237:1-6.
25. Sasou S, and Sugai T. Periarterial lymphoid sheath in the rat spleen: a light, transmission, and scanning electron microscopic study. Anat Rec 1992; 232:15-24.
26. van Krieken JH, Te Velde J, Kleiverda K, Leenheers-Binnendijk L, and van de Velde CJ. The human spleen; a histological study in splenectomy specimens embedded in methylmethacrylate. Histopathology 1985; 9:571-585.
27. van Krieken JH, and te Velde J. Normal histology of the human spleen. Am J Surg Pathol 1988; 12:777-785.
28. Saitoh K, Kamiyama R, and Hatakeyama S. A scanning electron microscopic study of the boundary zone of the human spleen. Cell tissue Res 1982; 222:655-665.
29. Fukuda T. Deep lymphatics of the spleen. Tohoku J Exp Med 1963; 79:281-292.
30. McGregor DD. Studies by thoracic duct drainage of the functions and potentialities of the lymphocyte. Fed Proc 1966; 25:1713-1719.
31. Dineen JK, and Adams DB. The effect of long-term lymphatic drainage on the lympho-myeloid system in the guinea-pig. Immunology 1970; 19:11-30.
32. Martin F, and Kearney JF. Marginal-zone B cells. Nat Rev Immunol 2002; 2:323-335.
33. Gray D, MacLennan IC, Bazin H, and Khan M. Migrant mu^+ $delta^+$ and static mu^+ $delta^-$ B lymphocyte subsets. Eur J Immunol 1982; 12:564-569.
34. Kumararatne DS, and MacLennan IC. Cells of the marginal zone of the spleen are lymphocytes derived from recirculating precursors. Eur J Immunol 1981; 11:865-869.
35. Kumararatne DS, Bazin H, and MacLennan IC. Marginal zones: the major B cell compartment of rat spleens. Eur J Immunol 1981; 11:858-864.
36. Weller S, Braun MC, Tan BK, Rosenwald A, Cordier C et al. Human blood IgM "memory" B cells are circulating splenic marginal zone B cells harboring a prediversified immunoglobulin repertoire. Blood 2004; 104:3647-3654.
37. Steiniger B, Timphus EM, and Barth PJ. The splenic marginal zone in humans and rodents: an enigmatic compartment and its inhabitants. Histochem Cell Biol 2006; 126:641-648.

Original Contribution

Kurume Medical Journal, 57, 21-28, 2010

Cerebrospinal Fluid following Cerebral Ischemia Accelerates the Proliferation of Bone Marrow Stromal Cells *in vitro*

KIMIHIKO ORITO*, †, HIDEKI HARADA**, †, MASATO HARA**, †,
SHINE YAMASHITA*, KIYOSHI KIKUCHI*
AND MINORU SHIGEMORI*

Departments of Neurosurgery and Anethesiology**, Kurume University School of Medicine and Neuroanesthesia Research Laboratory, Cognitive and Molecular Institute of Brain Diseases, Kurume University, Kurume 830-0011, Japan*

Received 15 December 2009, accepted 3 February 2010

Edited by TAKASHI HASHIMOTO

Summary: The central nervous system in the embryo develops around the cerebrospinal fluid (CSF), which regulates cell proliferation and differentiation. Neurogenesis has been also reported in the subventricular zone (SVZ), which is close to CSF, after stroke in rats. In this study, CSF extracted following stroke in rats was added to bone marrow stromal cell (MSC) culture *in vitro*, and the proliferation and differentiation of MSCs were studied. Primary cultures of MSCs were obtained from 7-week-old Lewis rats and incubated in a plastic tissue culture flask. CSF was retrieved from other rats 48 hrs after 0, 15 and 75 min after middle cerebral artery occlusion (MCAO). CSF from these three groups were added to respective MSC culture solutions, and the cells were then incubated for 72 hrs. Western blots of the extracellular signal-regulated kinase-1 and -2 (Erk1/2) were obtained just after the CSF induction. The expressions of CD34, CD45, CD90 and CD108 were assessed by flow cytometric analysis. The proliferation of MSCs was accelerated by the addition of post-stroke CSF, especially in the 15-min MCAO, in a dose-dependent manner. The morphology and surface antigens of the cells were maintained in all groups. Phosphorylated-Erk1/2 was elevated in all the CSF-treated groups, although this effect was more enhanced in the 15-min MCAO group. Our data indicate that the addition of post-stroke CSF to the primary medium stimulated the proliferation of MSCs, and that these MSCs maintained their characteristics through the p-Erk1/2 pathway. These results suggest that use of post-stroke CSF as a component of culture media could facilitate the autologous transplantation of MSCs.

Key words cerebrospinal fluid, cerebral ischemia, bone marrow stromal cells

INTRODUCTION

Many investigators have reported that intrathecal or intravenous administration of bone marrow stromal cell (MSCs) is an effective tool in functional recovery after stroke in rats [1,2]. The proliferation and differentiation of MSCs in response to growth factors such as epidermal growth factor (EGF) [3] and basic fibroblast growth factor (FGF2) [4] have been studied *in vitro*. However, the central nervous system develops around a fluid-filled compartment in the embryo, and the cerebral cortex in particular develops from the germinal epithelium adjacent to the cerebrospinal fluid (CSF), which helps regulate cell proliferation and differentiation [5]. CSF appears to contain large quantities of proteins, including growth factors, especially during development [6], as compared with only trace levels in adult CSF [7]. Historically, CSF stud-

Corresponding author: Kimihiko Orito, Department of Neurosurgery, Kurume University School of Medicine, 67 Asahi-machi, Kurume 830-0011, Japan. Tel: 0942-35-3311 Fax: 0942-37-1403 E-mail: orito_kimihiko@kurume-u.ac.jp

Abbreviations: CSF, cerebrospinal fluid; MCAO, middle cerebral artery occlusion; MSCs, bone marrow stromal cell; SVZ, subventricle zone.

ied in the context of the adult brain has been associated with mechanical functions and some simple physiological functions, but it is becoming increasingly clear that the CSF plays a much more critical physiological role [5,8-10].

By contrast, neurogenesis has been reported in the sub ventricle zone (SVZ) after stroke in rats [11], suggesting that the mature brain maintains the potential for neuronal replacement at the area near the CSF-filled cerebral ventricle [12]. The number of cells immunoreactive to Doublecortin, a marker for immature neurons, increased in the ipsilateral SVZ and striatum after stroke [13,14]. In addition, Doublecortin-positive cells generated in the SVZ migrated in a chainlike structure toward the ischemic striatum [15,16]. The areas which are recognized as sites of neurogenesis in the adult brain are the forebrain SVZ, hippocampus, and olfactory bulb, etc. Such brain parts are in close proximity to CSF. It is expected that the physical-spatial relationship with CSF could have a certain amount of control over progenitor cell and/or stem cell maintenance, proliferation and differentiation.

These findings focused our attention on the potential role of CSF following sublethal and/or lethal cerebral ischemia in the regulation of proliferation and differentiation of progenitor and/or stem cells, especially for intrathecal transplanted MSCs. In this study, CSF extracted 48 hrs after transient middle cerebral artery occlusion (MCAO), was added to MSC cultures *in vitro*, and the proliferation and differentiation of MSCs was examined.

MATERIALS AND METHODS

The study was approved by the Institutional Animal Care and Use Committee of Kurume University School of Medicine. All the experimental procedures were performed in line with Committee-issued guidelines.

Isolation and expansion of MSCs

Primary cultures of MSCs were obtained from the femur bone of 7-week-old Lewis rats (250-280 g). The bilateral femurs and tibias were aseptically dissected and the bones were cut off. The marrow was extruded with the culture medium into a flask and the cells from the marrow aspirates suspended in minimum essential medium (α-MEM, Gibco life Technology) supplemented with 20% fetal bovine serum (FBS, MP biomedical) were seeded onto a plastic tissue culture flask and incubated, and finally cultured in 5% CO^2 at 37 °C. After 48 hrs, the nonadherent cells were removed by changing the medium. When the cells grew until confluent, they were lifted using 0.25% trypsin and 0.02% EDTA in phosphate-buffered saline (PBS). The cells were cultured at a density of $5\text{-}10\times10^5$ cells/cm^2 and used in all the experiments.

Preparation of CSF retrieved from MCAO rats

Transient MCA occlusion

Other 7-week-old Lewis rats were prepared for the MCAO model for retrieval of CSF after stroke. A Laser-Doppler flow (LDF) probe attached to a flowmeter (ALF-21; Advance) was affixed to a dissected pocket made from scalp and subtemporal muscle, over the MCA area, to obtain a continuous measure of relative CBF in order to construct the MCAO model [17]. Then the rat was placed prone in a custom-built stereotaxic holder and prepared for MCAO via the intraluminal filament method. Briefly, the right common carotid artery was isolated from the surrounding fascia. The right external carotid artery was ligated and a silicone-coated nylon filament was inserted through the common carotid artery, into the internal carotid artery, and advanced until the LDF value was decreased by 20-30% of the basic value [17] so that MCAO was achieved, and this was maintained for 0 (n=10), 15 (n=10) or 75 (n=10) min. All the rats were awakened after the ischemic period; the CSF was retrieved 48 hrs after reperfusion. We fixed the head of the re-anesthetized rats to a frame, made a middle incision to the posterior cervical lesion, and ablated the cervical muscles. The foramen magnum was exposed and a PE-10 tube was cannulated for sampling CSF. Then 5-10 μl of CSF was retrieved from each rat, collected by group, and stored in a refrigerator at −80 degree Celsius. After retrieving the CSF, the rats were sacrificed, and the infarction volume was confirmed using TTC-stained brain sections to verify that MCAO had been successfully achieved.

Analysis of MSC expansion in various media

The third passage (P3) of 1.5×10^5 cells was cultured in 24 well plates under varying media conditions, essentially containing 0.5 ml of the standard cultivation-medium consisting of alpha-MEM supplemented with 20% fetal bovine serum, 1% glutamine, and 1% Penicillin/Streptomycin. Then 20 microliters from each of the three CSF groups were added to culture solutions and incubated for 24-72 h to assess the expansion, and then the number of cells was counted at 0 h, 24 h, 48 h, and 72 h after CSF induction, using the cell counter system. Dose dependence was also examined using 2, 5, or 10 microliters of CSF retrieved af-

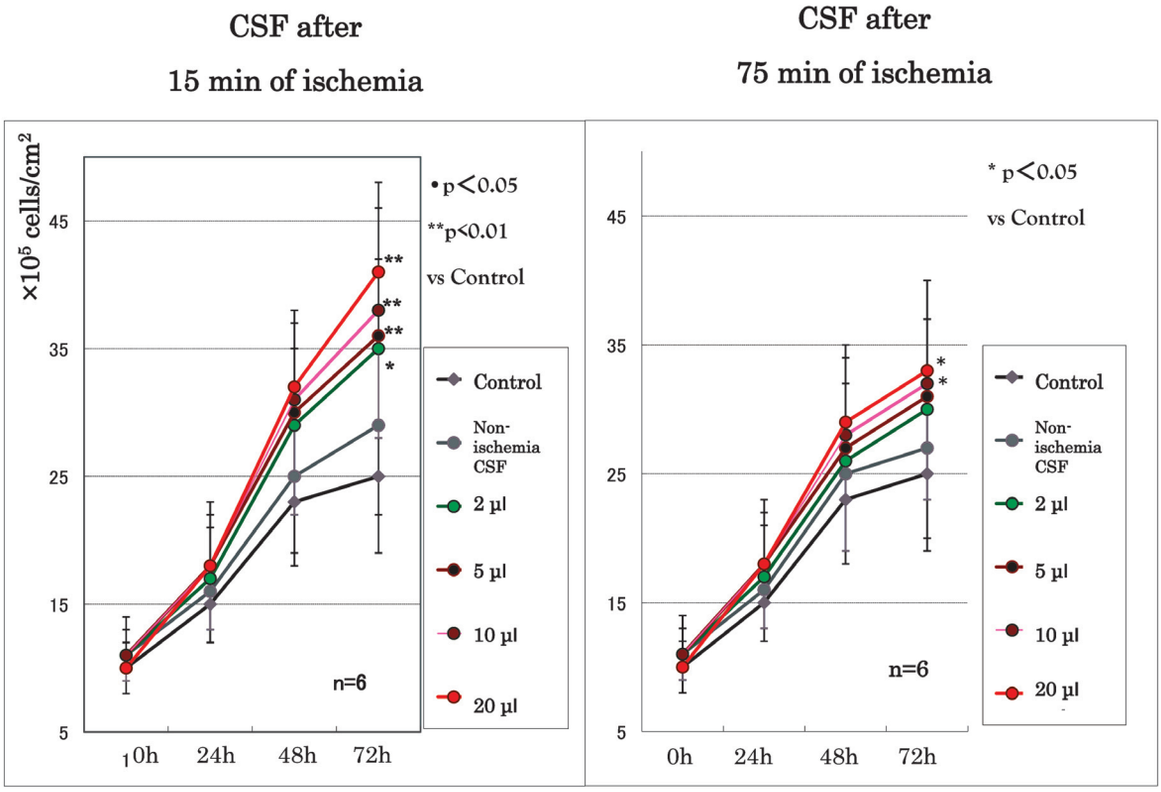
CSF after
15 min of ischemia
CSF after
75 min of ischemia
×10⁵ cells/cm²
45
35
25
15
5
0h
24h
48h
72h
•p<0.05
**p<0.01
vs Control
n=6
Control
Non-ischemia CSF
2 µl
5 µl
10 µl
20 µl
* p<0.05
vs Control

Fig. 1.

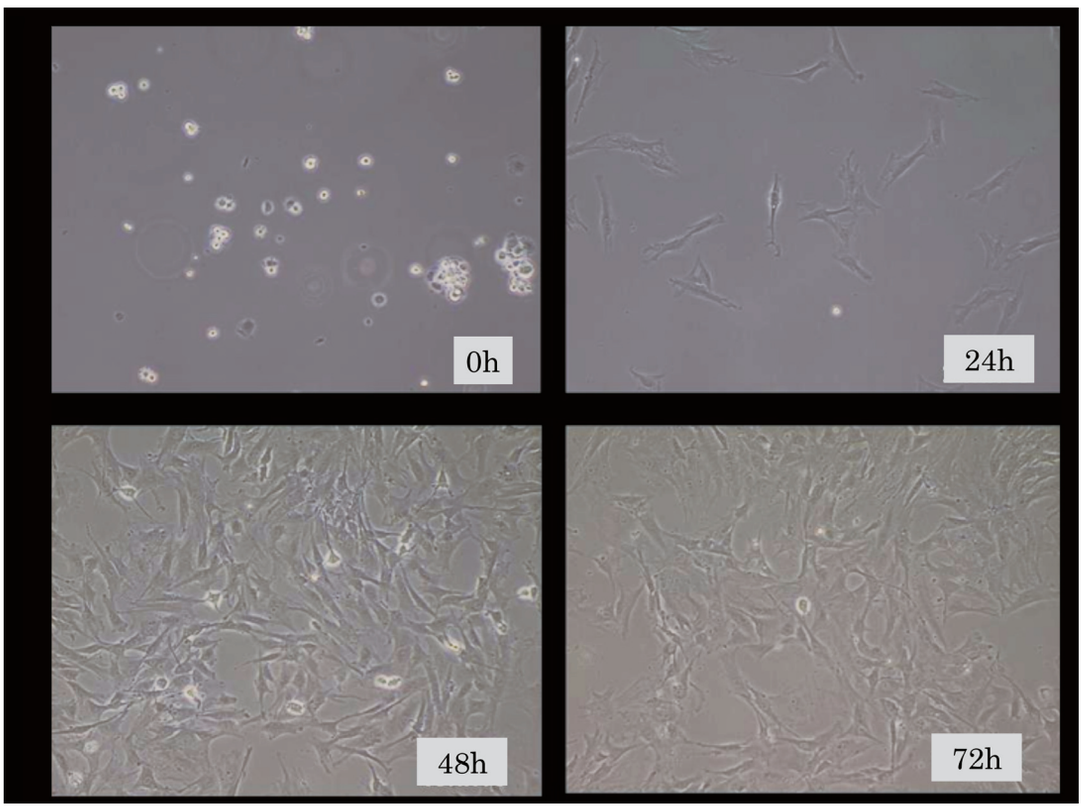
0h
24h
48h
72h

Fig. 2.

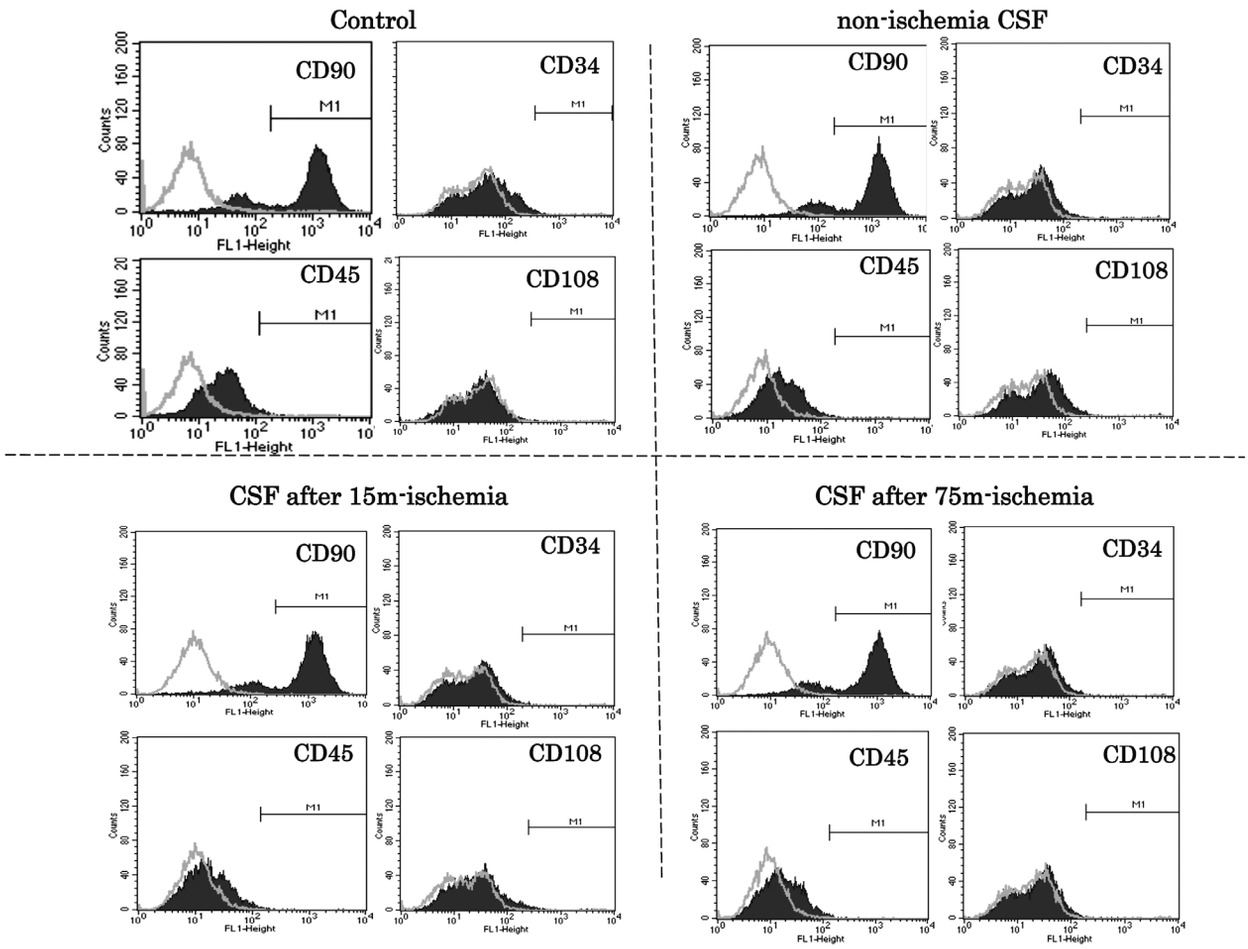
Control
non-ischemia CSF
CSF after 15m-ischemia
CSF after 75m-ischemia
CD90
CD34
CD45
CD108
M1
Counts
FL1-Height

Fig. 3.

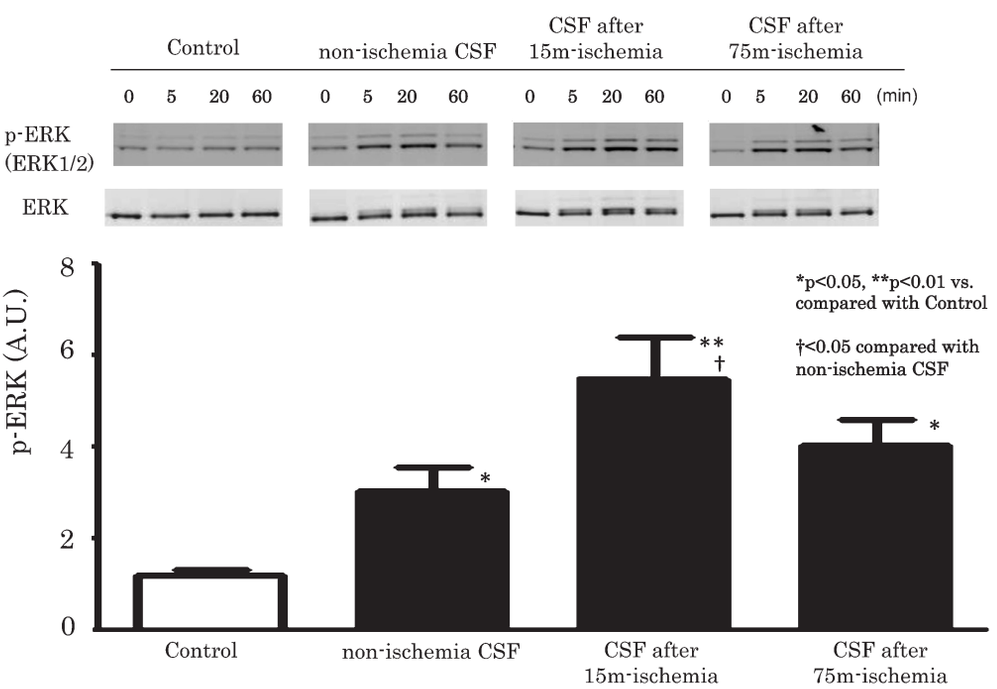
Control
non-ischemia CSF
CSF after 15m-ischemia
CSF after 75m-ischemia
0 5 20 60 0 5 20 60 0 5 20 60 0 5 20 60 (min)
p-ERK (ERK1/2)
ERK
p-ERK (A.U.)
*p<0.05, **p<0.01 vs. compared with Control
†<0.05 compared with non-ischemia CSF

Fig. 4.

ter cerebral ischemia.

Phenotypic analysis of MSCs

The expanded cells were characterized at 72 hrs after CSF induction by flow cytometric analysis of specific surface antigens. Cells were incubated for 30 min at room temperature, with fluorescein isothiocyanate (FITC) or phycoerythin (PE)-conjugated primary antibody. Then, in the case of unconjugated primary antibodies, they were washed in PBS buffer and incubated for 30 min at room temperature with a second FITC or PE-conjugated antibody [anti-F $(ab')_2$ mouse-FITC/PE, Dako, Glostrup, Denmark]. The expression of antigens CD34, CD45, CD90 and CD108 (Beckman Coulter, Tokyo, Japan) was measured by flow cytometric analysis with a Coulter EPICS XL (Coulter, Miami, FL, USA).

Western blotting of Erk1/2

Antibodies were obtained from commercial sources: for Erk and p-Erk antibodies (New England Biolabs, Ipswich, MA). For the Western blot analysis, the cells were rinsed with PBS and subsequently lysed for 30 min on ice in RIPA-B buffer (0.5% Nonidet P-40, 20 mM Tris, pH 8.0, 50 mM NaCl, 50 mM NaF, 100 M Na3VO4, 1 mM DTT, and 50 g/ml PMSF). The insoluble material was removed by centrifugation at 12,000 rpm for 20 min, at 4 °C. Next, the supernatant was subjected to SDS-PAGE, and Western blot analysis was performed. Equal amounts of protein were subjected to SDS-polyacrylamide gel electrophoresis and transferred to the nitrocellulose membranes. The blots were blocked in PBS with 5% skim milk and 0.05% Tween 20, incubated with the appropriate antibodies, and subsequently incubated with the secondary antibodies conjugated with horseradish peroxidase. Next, the blots were assayed by enhanced chemiluminescence detection (Amersham Biosciences, Piscataway NJ).

Statistical analysis

The data were analyzed by one-factor analysis of variance (ANOVA) followed by the post hoc Fisher's PLSD test and Newman-Keuls test. These statistical analyses were performed with Statview for Macintosh version 5.0, and $P<0.05$ was considered statistically significant.

RESULTS

Isolation and enumeration of MSCs after the induction of additional CSF culture

The growth rate was faster in cells cultured with CSF after MCAO than in the controls (Fig. 1). However, the cells of all the groups were observed to be similar, meeting all the criteria of morphology for MSCs, e.g. plastic adherence, and spindle shape. When compared with the control group, a significantly larger increase in proliferation of MSCs was observed in CSF after 15 min of ischemia, as compared with CSF after 75 min of ischemia. When the amount of CSF was progressively decreased from 20 to 10, 5 and 2 microliters, the proliferation rate decreased in a CSF volume-dependent manner.

Characterization of MSCs by flow cytometry

The majority of MSCs expanded in all the media investigated were clearly distinguishable from hematopoietic cells by the absence of the hematopoietic markers CD34, CD45, CD108 and CD90 typically expressed by MSCs. The addition of CSF did not affect the quality of the MSCs in any group (Fig. 3). This indicates that the phenotype of these cells was identical to the phenotype described for MSCs.

Activation of ErK1/2 pathways after treatment with CSF

Phosphorylation of ErK1/2 was investigated in all the CSF-treated groups; however, CSF after 15 min of ischemia showed especially potent phosphorylation of ErK1/2 in Western blotting analysis. The amount of phospho-ErK1/2 at 60 min was elevated in all the CSF-treated groups; however, it was more enhanced in the group receiving CSF obtained after 15 min of ischemia (Fig. 4).

DISCUSSION

This study reports several new findings: (1) adding CSF retrieved after cerebral ischemia to primary medium accelerates the proliferation of MSCs, and this effect is more potent with CSF obtained after a relatively shorter cerebral ischemic duration; (2) the morphology and the surface antigen characteristics of MSCs were maintained after culture with CSF; and (3) use of CSF increases phosphorylation of the Erk, especially in CSF obtained after a relatively short ischemic duration.

CSF after cerebral ischemia accelerates the proliferation of MSCs

Several growth factors are known to be secreted by the choroid plexus directly into the CSF, which is vital to the developmental process, especially in the

developing brain [6,5]. Therefore, CSF could play a critical role in the development of stem or/and progenitor cells such as MSCs. Gato et al. [18] demonstrated that slices of developing chick brain were incapable of supporting neurogenesis from the germinal epithelium unless CSF was added to the growth medium. Miyan et al. [5] also stated that rather than critical growth factors being produced in the local microenvironment of the brain, the surrounding CSF is sufficient to drive the developmental process.

Neurogenesis however, has been reported in SVZ after stroke in rats [19-21], suggesting that the mature brain maintains the potential for neuronal replacement in the area close to the CSF- filled cerebral ventricle.

Although naïve CSF activated ErK1/2, it showed no potency to stimulate MSC proliferation in our study. This suggests that cerebral ischemia might mimic conditions in the proto-brain during the early brain development period, and activate the proliferation of progenitor cells in areas surrounding the ventricle, such as the SVZ.

Consistent morphology and surface antigen characteristics of the MSCs

Cells expanded by our protocol meet all the criteria for MSCs, e.g. plastic adherence, spindle-shaped morphology, and surface marker expression [22]. During the expansion of MSCs in classical α-MEM, it is established that these cells lose both their multipotentiality and renewal capacity with successive passages [23]. In our study, the addition of CSF medium had no effect on the morphology and phenotype of MSCs cultured for 72 hrs following induction, although ErK1/2 was activated. MSCs are known to be multipotent, capable of differentiating into at least three lineages (osteogenic, chondrogenic, and adipogenic), when cultured under defined *in vitro* conditions. [24,25] Jaiswal et al. [26] reported a potential mechanism involving MAP-kinase activation in the osteogenic differentiation of adult stem cells and suggested that the commitment of hMSCs into osteogenic or adipogenic lineages is governed by the activation or inhibition of ErK. Jori et al. [27] has also reported that MEK-ErK signaling could contribute to neural commitment and differentiation *in vitro* in marrow stromal stem cells. The absence of any effect of ErK activation in the present study could be because the culture duration in our study was too short for differentiation of the MSCs after the CSF treatment. We need an extended culture-duration to observe the capability of these MSCs to differentiate into various lineages.

Additional CSF increases the phosphorylation of the Ras-MEK-Erk pathway, especially in the shorter ischemic time group

In this study, the phospho-ErK1/2 protein level increased in CSF–treated MSCs within 5 to 60 min after onset of the induction. Further, ErK1/2 was especially enhanced in cells receiving CSF from rats in the 15-minute ischemic time group. MAPK/Erk1/2 is an important signal transduction pathway that affects a wide range of cell activities, including cell proliferation, cell survival and cell death. It is well known that sublethal ischemia leads to significant protection as ischemic preconditioning (IPC), in a rodent model subjected to lethal ischemia [28-30]. Lee et al. [11] reported that IPC enhances neurogenesis in the SVZ even without subsequent lethal ischemia. Maysami et al. [31] also reported that neurogenesis in the brain occurs after brief ischemia, resulting in preconditioning, and attenuation of ischemia-induced endogenous progenitor cell proliferation in the brain blocked the induction of ischemic tolerance. Erk activation after preconditioning ischemia is also reported as one of the protective responses in ischemic tolerance [32,33]. In our study, sublethal ischemia led to increased activation of the Erk pathway in MSCs cultured with CSF. Considering that endogenous progenitor cells in the SVZ are close to the CSF-filled ventricle, we might speculate that some cytokines, including growth factors, are secreted by the choroid plexus after ischemia directly into CSF, similar to what occurs during the developmental process, and then stimulate the progenitor cells, which is in part one of the key mechanisms in IPC.

To conclude, addition to the primary medium of CSF retrieved after cerebral ischemia accelerates the proliferation of MCSs, especially in the case of CSF retrieved after relatively short-duration MCAO, and cultured cells maintain the morphology and surface antigen characteristics of MSCs. Addition of CSF increases the phosphorylation of the Erk pathway, especially for CSF obtained after a short-duration MCAO. These findings suggest that addition of CSF after stroke to cell culture medium could be useful in autologous transplantation of MSCs. The finding that CSF obtained after short-term ischemia has a more potent proliferative effect than CSF after longer-term ischemia could be an important key in helping to unlock the mechanism of ischemic preconditioning in the brain.

REFERENCES

1. Chen J, Li Y, Katakowski M, Chen X, Wang L et al.

Intravenous bone marrow stromal cell therapy reduces apoptosis and promotes endogenous cell proliferation after stroke in female rat. J Neurosci Res 2003; 73:778-786.
2. Pavlichenko N, Sokolova I, Vijde S, Shvedova E, Alexandrov G et al. Mesenchymal stem cells transplantation could be beneficial for treatment of experimental ischemic stroke in rats. Brain Res 2008; 1233:203-213.
3. Sato H, Kuwashima N, Sakaida T, Hatano M, Dusak JE et al. Epidermal growth factor receptor-transfected bone marrow stromal cells exhibit enhanced migratory response and therapeutic potential against murine brain tumors. Cancer Gene Ther 2005; 12:757-768.
4. Bhang SH, Lee YE, Cho SW, Shim JW, Lee SH et al. Basic fibroblast growth factor promotes bone marrow stromal cell transplantation-mediated neural regeneration in traumatic brain injury. Biochem Biophys Res Commun 2007; 359:40-45.
5. Miyan JA, Zendah M, Mashayekhi F, and Owen-Lynch PJ. Cerebrospinal fluid supports viability and proliferation of cortical cells in vitro, mirroring in vivo development. Cerebrospinal Fluid Res 2006; 3:2.
6. Miyan JA. Nabiyouni M, and Zendah M. Development of the brain: a vital role for cerebrospinal fluid. Can J Physiol Pharmacol 2003; 81:317-328.
7. Gato A, Martin P, Alonso MI, Martin C, Pulgar MA et al. Analysis of cerebro-spinal fluid protein composition in early developmental stages in chick embryos. J Exp Zoolog A Comp Exp Biol 2004; 301:280-289.
8. Owen-Lynch PJ, Draper CE, Mashayekhi F, Bannister CM, and Miyan JA. Defective cell cycle control underlies abnormal cortical development in the hydrocephalic Texas rat. Brain 2003; 126:623-631.
9. Mashayekhi F, Draper CE, Bannister CM, Pourghasem M, Owen-Lynch PJ et al. Deficient cortical development in the hydrocephalic Texas (H-Tx) rat: a role for CSF. Brain 2002; 125:1859-1874.
10. Miyan JA, Mashayekhi F, and Bannister CM. Developmental abnormalities in early-onset hydrocephalus: clues to signalling. Symp Soc Exp Biol 2001:91-106.
11. Lee SH, Kim YJ, Lee KM, Ryu S, and Yoon BW. Ischemic preconditioning enhances neurogenesis in the subventricular zone. Neuroscience 2007; 146:1020-1031.
12. Darsalia V, Heldmann U, Lindvall O, and Kokaia Z. Stroke-induced neurogenesis in aged brain. Stroke 2005; 36:1790-1795.
13. Ling L, Hou Q, Xing S, Yu J, Pei Z et al. Exogenous kallikrein enhances neurogenesis and angiogenesis in the subventricular zone and the peri-infarction region and improves neurological function after focal cortical infarction in hypertensive rats. Brain Res 2008; 1206:89-97.
14. Thored P, Wood J, Arvidsson A, Cammenga J, Kokaia Z et al. Long-term neuroblast migration along blood vessels in an area with transient angiogenesis and increased vascularization after stroke. Stroke 2007; 38:3032-3039.
15. Kobayashi T, Ahlenius H, Thored P, Kobayashi R, Kokaia Z et al. Intracerebral infusion of glial cell line-derived neurotrophic factor promotes striatal neurogenesis after stroke in adult rats. Stroke 2006; 37:2361-2367.
16. Zhang PB, Liu Y, Li J, Kang QY, Tian YF et al. Ependymal/subventricular zone cells migrate to the peri-infarct region and differentiate into neurons and astrocytes after focal cerebral ischemia in adult rats. Di Yi Jun Yi Da Xue Xue Bao 2005; 25:1201-1206.
17. Harada H, Wang Y, Mishima Y, Uehara N, Makaya T et al. A novel method of detecting rCBF with laser-Doppler flowmetry without cranial window through the skull for a MCAO rat model. Brain Res Brain Res Protoc 2005; 14:165-170.
18. Gato A, Moro JA, Alonso MI, Bueno D, and De La Mano A. Embryonic cerebrospinal fluid regulates neuroepithelial survival, proliferation, and neurogenesis in chick embryos. Anat Rec A Discov Mol Cell Evol Biol 2005; 284:475-484.
19. Parent JM, Vexler ZS, Gong C, Derugin N, and Ferriero DM. Rat forebrain neurogenesis and striatal neuron replacement after focal stroke. Ann Neurol 2002; 52:802-813.
20. Parent JM. Injury-induced neurogenesis in the adult mammalian brain. Neuroscientist 2003; 9:261-272.
21. Zhang R, Zhang Z, Wang L, Wang Y, Gousev A et al. Activated neural stem cells contribute to stroke-induced neurogenesis and neuroblast migration toward the infarct boundary in adult rats. J Cereb Blood Flow Metab 2004; 24:441-448.
22. Lange C, Cakiroglu F, Spiess AN, Cappallo-Obermann H, Dierlamm J et al. Accelerated and safe expansion of human mesenchymal stromal cells in animal serum-free medium for transplantation and regenerative medicine. J Cell Physiol 2007; 213:18-26.
23. Meuleman N, Tondreau T, Delforge A, Dejeneffe M, Massy M et al. Human marrow mesenchymal stem cell culture: serum-free medium allows better expansion than classical alpha-MEM medium. Eur J Haematol 2006; 76:309-316.
24. Bruder SP, Fink DJ, and Caplan AI. Mesenchymal stem cells in bone development, bone repair, and skeletal regeneration therapy. J Cell Biochem 1994; 56:283-294.
25. Pittenger MF, Mackay AM, Beck SC, Jaiswal RK, Douglas R et al. Multilineage potential of adult human mesenchymal stem cells. Science 1999; 284:143-147.
26. Jaiswal RK, Jaiswal N, Bruder SP, Mbalaviele G, Marshak DR et al. Adult human mesenchymal stem cell differentiation to the osteogenic or adipogenic lineage is regulated by mitogen-activated protein kinase. J Biol Chem 2000; 275:9645-9652.
27. Jori FP, Napolitano MA, Melone MA, Cipollaro M, Cascino A et al. Molecular pathways involved in neural in vitro differentiation of marrow stromal stem cells. J Cell Biochem 2005; 94:645-655.
28. Kitagawa K, Matsumoto M, Tagaya M, Hata R, Ueda H et al. 'Ischemic tolerance' phenomenon found in the brain. Brain Res 1990; 528: 21-24.
29. Taga K, Patel PM, Drummond JC, Cole DJ, and Kelly PJ. Transient neuronal depolarization induces tolerance to subsequent forebrain ischemia in rats. Anesthesiology 1997; 87:918-925.
30. Davis DP, and Patel PM. Ischemic preconditioning in the brain. Curr Opin Anaesthesiol 2003; 16:447-452.
31. Maysami S, Lan JQ, Minami M, and Simon RP. Proliferating progenitor cells: a required cellular element for induction of ischemic tolerance in the brain. J Cereb Blood Flow

Metab 2008; 28:1104-1113.
32. Gu Z, Jiang Q, and Zhang G. Extracellular signal-regulated kinase and c-Jun N-terminal protein kinase in ischemic tolerance. Neuroreport 2001; 12:3487-3491.
33. Choi JS, Kim HY, Cha JH, and Lee MY. Ischemic preconditioning-induced activation of ERK1/2 in the rat hippocampus. Neurosci Lett 2006; 409:187-191.

Original Contribution

Kurume Medical Journal, 57, 29-38, 2010

Methylphenidate Enhances Inhibitory Synaptic Transmission by Increasing the Content of Norepinephrine in the Locus Coeruleus of Juvenile Rats

YURI KIDANI*, MASARU ISHIMATSU*,** AND TAKASHI AKASU*,**

**Department of Physiology, Kurume University School of Medicine and*
***Cognitive and Molecular Research Institute of Brain Diseases,*
Open Research Center, Kurume University,
Kurume 830-0011, Japan

Received 14 December 2009, accepted 17 February 2010

Edited by TAKAYUKI TANIWAKI

Summary: The present study examined the effect of methylphenidate (MPH), a psychostimulant, on noradrenergic transmission in the locus coeruleus (LC) of juvenile rats. Intracellular recordings showed that MPH (>3 μM) produced a hyperpolarizing response associated with a decrease in the rate of spontaneously firing action potentials. MPH (1 μM) enhanced the amplitude of the inhibitory postsynaptic potential (IPSP) mediated by norepinephrine (NE), but did not change the excitatory postsynaptic potential (EPSP) mediated by excitatory amino acids. Whole-cell patch-clamp recordings showed that MPH (0.3-30 μM) produced an outward current (I_{MPH}) and enhanced the inhibitory postsynaptic current (IPSC) in neurons of the juvenile rat LC. MPH (30 μM) enhanced the NE-induced outward current (I_{NE}). Bath-application of yohimbine (1 μM) produced an inward current and blocked the MPH-induced enhancement of the IPSC. Yohimbine (1 μM) depressed not only the I_{NE} but also the I_{MPH} in juvenile rat LC neurons. The current-voltage relationship of the I_{MPH} showed inward rectification and reversed polarity at −91.1±4.3 mV (n=5). Ba^{2+} (100 μM) blocked the I_{MPH}, indicating that the I_{MPH} is mediated by Ba^{2+}-sensitive inward rectifier K^+ current. These results suggest that MPH enhances inhibitory synaptic transmission by increasing the concentration of NE at noradrenergic synapses in juvenile rat LC neurons.

Key words methylphenidate, norepinephrine transporter, outward current, NE transmission, IPSC, locus coeruleus, juvenile rats, ADHD

INTRODUCTION

Methylphenidate (MPH) is clinically beneficial for the treatment of patients with attention-deficit hyperactivity disorder (ADHD) who exhibit neuropsychiatric symptoms, including inattention, hyperactivity and variable impulsiveness, typically of juvenile onset [1-4]. The pathophysiology of ADHD is unclear, but research has focused on the possible dysfunction of norepinephrine (NE) and/or dopamine (DA) neurons in the central nervous system (CNS) [1,3,5]. Selective monoamine re-uptake inhibitors, α_2-adrenergic agonists and tricyclic antidepressants alleviate the clinical symptoms of ADHD [6,7]. Activation of presyn-

Correspondence to Prof. Takashi Akasu, Department of Physiology, Kurume University School of Medicine, 67 Asahi-machi, Kurume 830-0011, Japan Tel: +81-942-31-7543 Fax: +81-942-31-7728 E-mail: akasut@med.kurume-u.ac.jp

Abbreviations: ACSF, artificial cerebrospinal fluid; ADHD, attention-deficit hyperactivity disorder; CNS, central nervous system; DA, dopamine; DAT, DA transporters; EGTA, ethylene glycol-bis(β-aminoethyl ether)-N,N,N',N'-tetraacetic acid; EPSC, excitatory postsynaptic current; EPSP, excitatory postsynaptic potential; GABA, γ-aminobutyric acid; GTP, guanosine 5'-triphosphate; HEPES, N-(2-hydroxyethyl)piperazine-N'-(2-ethanesulfonic acid); PFC, prefrontal cortex; PSCs, postsynaptic currents; I_{MPH}, MPH-induced outward current; I_{NE}, NE-induced outward current; IPSC, inhibitory postsynaptic current; IPSP, inhibitory postsynaptic potential; I-V, current-voltage; LC, locus coeruleus; ATP, adenosine 5'-triphosphate; MPH, methylphenidate; NE, norepinephrine; NET, NE transporters; Vh., holding membrane potential.

aptic α_2-autoreceptors impairs attention and target detection by reducing the release of NE [8,9]. It has been known that MPH, as an inhibitor of both NE transporters (NET) and DA transporters (DAT), improves the working memory and attentional functions in rats by increasing the release of catecholamine [10-12]. Recently, administration of MPH, at low concentrations, preferentially increased catecholamine neurotransmission within the prefrontal cortex (PFC), enhancing cognitive function [12]. However, few studies have examined the effect of MPH on noradrenergic synaptic transmission in the CNS, *in vitro*.

The locus coeruleus (LC) is a central noradrenergic nucleus that sends numerous projections widely in the mammalian CNS [13,14]. The LC participates in various brain functions, including vigilance, attention and mediation of stress response [15-17]. Previous studies showed that administration of MPH to LC neurons reduced the firing rate of spontaneous action potentials, *in vivo* [16,18]. Recently, MPH has been shown to produce a hyperpolarizing response (and an outward current) via activation of α_2-adrenoceptors, and to enhance the inhibitory postsynaptic potential (IPSP) in adult rat LC neurons [19,20]. The LC is particularly useful for studying the function of noradrenergic synaptic transmission because recurrent collaterals of LC neurons release NE onto the somatodendritic membrane of other (or the soma) LC neurons, mediating the IPSP [21]. The purpose of the present study was to examine the effect of MPH on the IPSP in LC neurons of juvenile rats by intracellular and whole-cell patch-clamp recording methods. Preliminary findings of this work have appeared in abstract form [22].

MATERIALS AND METHODS

Brain slices containing the LC were obtained from Wistar-Kyoto (WKY) rats in a manner described previously [19,23]. Briefly, juvenile male rats (within 1 W after birth, 50-100 g) were killed by decapitation under anesthesia with pentobarbital (40 mg/kg), and their brains were rapidly removed and immersed for 8-10 s in a cooled (4°C) artificial cerebrospinal fluid (ACSF) that was pre-bubbled with 95% O_2-5% CO_2. Horizontal brain slices (200-250 μm in thickness) were cut with a VT1000S (Leica) in cooled ACSF and left to recover for one hour in oxygenated ACSF at room temperature (22-24°C). A hemisected slice was submerged in the ACSF (32-33°C) during the electrophysiological experiments. The composition of the ACSF was as follows (in mM): 126 NaCl, 2.5 KCl, 2.4 $CaCl_2$, 1.2 $MgCl_2$, 21 $NaHCO_3$, 1.2 $NaHPO_4$, and D-glucose pH 7.4 and 295-305 (mOsm). Intracellular recordings were made with glass microelectrodes filled with 2 M KCl (tip resistance 26-40 MΩ). Whole-cell tight-seal recordings were made from LC neurons using the slice patch-clamp technique [19]. Patch pipettes were filled with the internal solution (mM): 130 KCl, 20 NaCl, 0.3 $CaCl_2$, 1 $MgCl_2$, 1 ethylene glycol-bis(β-aminoethyl ether)-N,N,N',N'-tetraacetic acid (EGTA); 2 adenosine 5'-triphosphate (ATP); 0.25 guanosine 5'-triphosphate (GTP); and 10 N-(2-hydroxyethyl)piperazine-N'-(2-ethanesulfonic acid) (HEPES) (pH 7.3 adjusted by KOH, 280 mOsm). Tip resistance of the whole-cell patch-pipettes was 3-5 MΩ. A single focal stimulation (20-50 V for 200-300 μS) was applied to the lateral edge of the LC to evoke postsynaptic responses at intervals of 30 s [21]. Voltage and current were recorded with an Axoclamp-2A amplifier and were monitored continuously with an oscilloscope (Nihon-Kohden, RTA-1100). During the whole-cell patch-clamping, sample frequencies were between 4.5 and 6 kHz and the amplifier gain was 0.8-2.5 nA/mV. A pClamp system (Axon Instruments) operating on a Windows based PC was used to analyze the membrane potential and current. Drugs used were GTP, EGTA, NE, remoxipride, SCH23390, and yohimbine, all of which were purchased from Sigma-Aldrich Corporation (St. Louis, MO, USA). MPH hydrochloride was gift from NOVARTIS Pharma (Basel, Switzerland). SCH23390 were dissolved in ethanol and applied to the ACSF. Each experimental value was presented as the mean±SE and was analyzed by unpaired Student's *t*-test.

RESULTS

Effects of MPH on synaptic transmission in the juvenile rat LC

Neurons in the juvenile rat LC exhibited tonic firing of spontaneous action potentials with a frequency of 0.5 to 3 Hz, when impaled by an intracellular microelectrode (Fig. 1Aa). The resting membrane potential and input resistances of LC neurons were −54.0±2.0 mV (n=55) and 52.2±4.0 MΩ (n=55), respectively, when recorded during intervals in spontaneous spike activity. These activities of LC neurons in juvenile rats are comparable to those in adult rats [21,23]. Figure 1Aa shows the effect of MPH (10 μM) on the membrane potential of juvenile rat LC neurons. Bath-application of MPH (10 μM) for 5 min produced a hyperpolarizing response that lasted for 10-15 min and recovered within 20-30 min after withdrawal of MPH

from the superfusing solution. The MPH-induced hyperpolarization was associated with a decrease in the rate of spontaneous action potential rate. Figure 1Ab shows electrotonic potentials produced by injection of inward current pulses with a duration of 400 ms. MPH (10 μM) depressed the amplitude of electrotonic potentials, indicating that MPH (10 μM) decreased the input resistance of juvenile rat LC neurons. Bath-application of MPH (0.1-0.3 μM) to LC neurons produced no detectable hyperpolarization in 9 neurons. MPH (1 μM) produced a hyperpolarizing response with amplitude of 1-3 mV in 6 neurons, but not in the remaining 3 neurons. Altogether, the amplitude of the hyperpolarizing response produced by MPH (1 μM) was 1.3±0.8 mV (n=6). MPH at concentrations of 3, 10 and 30 μM produced hyperpolarizing responses with amplitudes of 6.3±2.7 mV (n=7), 8.2±1.3 mV (n=7) and 13.6±1.2 mV (n=11), respectively in juvenile rat LC neurons. We next examined the effect of MPH on noradrenergic synaptic transmission in the LC of juvenile rats (Fig. 1B). The IPSP was recorded at a membrane potential of −60 mV by continuous injection of hyperpolarizing DC current to block the spontaneous firing activity. Application of single focal stimulation to the rostral edge of the LC with intensity of 20 V evoked a potential sequence of the excitatory postsynaptic potential (EPSP) and the IPSP (Fig. 1Ba). Bath-application of MPH (1 μM) to the ACSF for 5 min increased the amplitude and the duration of the IPSP (Fig. 1Bb). The amplitude of the IPSP recovered within 20 min after withdrawal of MPH from the ACSF. However, the duration of the IPSP was not completely restored within the recovery time. In contrast, MPH (1 μM) did not change the amplitude of the EPSP in juvenile rat LC neurons (Fig. 1Bc). The effect of MPH on the IPSP was concentration-dependent (Table 1).

TABLE 1.
Effect of MPH on the amplitude of IPSPs in juvenile rat LC neurons

Concentration of MPH (μM)	Increase in IPSPs (%)
0.1	124± 8 (n=5)*
0.3	166±41 (n=5)*
1	198±26 (n=6)*
3	201±43 (n=6)*
10	163±33 (n=6)*

Data are expressed as mean±SE. The number of experiments is shown in parentheses. The asterisk indicates statistical significance by Student's *t*-test.

MPH (0.1 μM) produced a 124±8% (n=5) increase in the amplitude of the IPSP in juvenile rat LC neurons. MPH (0.3-10 μM) enhanced the amplitude of the IPSP in a concentration-dependent manner.

The effect of MPH on synaptic transmission in the juvenile rat LC was examined using voltage-clamp techniques, because the postsynaptic potentials are dependent on the membrane potential and resistance. Under whole-cell patch-clamp conditions, stimulation of the LC produced an excitatory postsynaptic current (EPSC) followed by an inhibitory postsynaptic current (IPSC) (Fig. 2Aa). The amplitude of the IPSC evoked by a stimulus intensity of 20 V was 28.3±8.0 pA (n=7) at −60 mV. Bath-application of MPH (1 μM) for 5 min produced no obvious outward current in the membrane current, but markedly increased the amplitude of IPSC to 47.1±5.7 pA (n=7) at the same holding potential. The duration of the IPSC was also increased by MPH

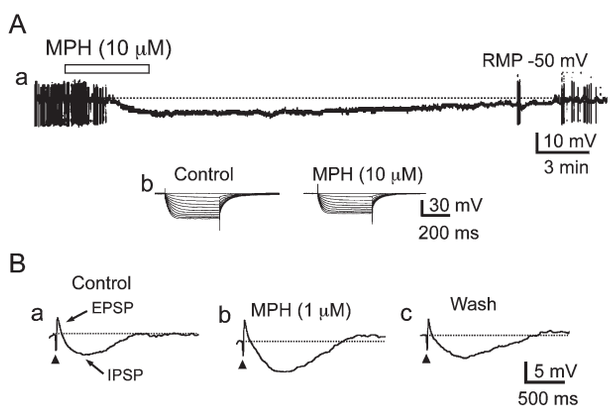

Fig. 1. Effects of MPH (1 μM) on the resting membrane potential and the postsynaptic potentials in juvenile rat LC neurons. (A) Upper trace (a) shows a sample record of the hyperpolarization induced by MPH (10 μM). The original resting membrane potential was −50 mV. Open horizontal bar indicates the period of bath-application of MPH. Upward and downward deflections indicate spontaneous action potentials. Lower traces (b) shows the effect of MPH (10 μM) on electrotonic potentials induced by hyperpolarizing current pulses with duration of 400 ms. Left and right traces were obtained before and 10 min after application of MPH (10 μM). (B) The effects of MPH (1 μM) on the potential sequence of the EPSP and the IPSP obtained at the membrane potential of −60 mV. Traces (a) and (b) were taken before and 10 min after application of MPH (1 μM). Trace (c) was obtained 30 min after withdrawal of MPH from the ACSF. Each trace was the sum of 6 responses. Ordinate indicates percent increase in the amplitude of the IPSP and the EPSP. Vertical line on each point indicates the mean±SE of mean. The number of experiments was shown in parentheses.

(1 μM). The effect of MPH (1 μM) on the EPSC was examined at a membrane potential of −90 mV in juvenile rat LC neurons. Since the IPSC partially overlapped the EPSC, the IPSC was eliminated at the membrane potential of −90 mV, the equilibrium potential of K ions [21]. MPH (1 μM) did not obviously change the amplitude and the duration of the EPSC in LC neurons (Fig. 2Ab). Pooled data showed that the amplitudes of the EPSC were 125.0±17.7 pA (n=2) and 129.7±9.1 pA (n=12) in the absence and the presence of MPH (1 μM), respectively. There was no statistical significance between these two figures ($p<0.1$). Figure 2B shows the effects of MPH (0.1-100 μM) on the amplitude of the EPSC and the IPSC in juvenile rat LC neurons. The effects of MPH on the IPSC showed a bell-shaped concentration-response relationship. MPH (0.3-10 μM) increased the amplitude of the IPSC in a concentration-dependent manner. The amplitude of the IPSC was enhanced to 232±35% (n=5) of control by MPH (10 μM). However, at a concentration of 30 μM, MPH produced only a 152±12% (n=10) enhancement of the IPSC. MPH (100 μM) conversely depressed the IPSC to 25% of the control level (n=4). In contrast to the IPSC, MPH (0.1-100 μM) did not significantly change the amplitude of the EPSC in juvenile rat LC neurons (Fig. 2B). Figure 3A shows the concentration-dependent effect of MPH (1-100 μM) on the time course of the IPSC obtained at a holding potential of −60 mV in juvenile rat LC neurons. MPH (10 μM) markedly enhanced both the amplitude and the duration of the IPSC (Fig. 3Aa). However MPH at a concentration of 30 μM did not obviously alter the peak amplitude of the IPSC, but markedly increased the duration of the IPSC (Fig. 3Ab). The concentration-response relationship between the duration of the IPSC and the concentration of MPH (1-30 μM) is shown in Fig. 3B. The rise time and the rate of decay of the IPSC were represented by the time-to-peak (t_1) and the half-decay time (t_2) of the IPSC, respectively. MPH (1 μM) increased both the (t_1) and (t_2) of the IPSC to 165±8% (n=6) of control and 156±10% (n=6) of control, respectively. At a concentration of 30 μM, MPH increased the (t_1) and (t_2) of the IPSC to 384±70% (n=6) and 511±90% (n=6) of the control, respectively.

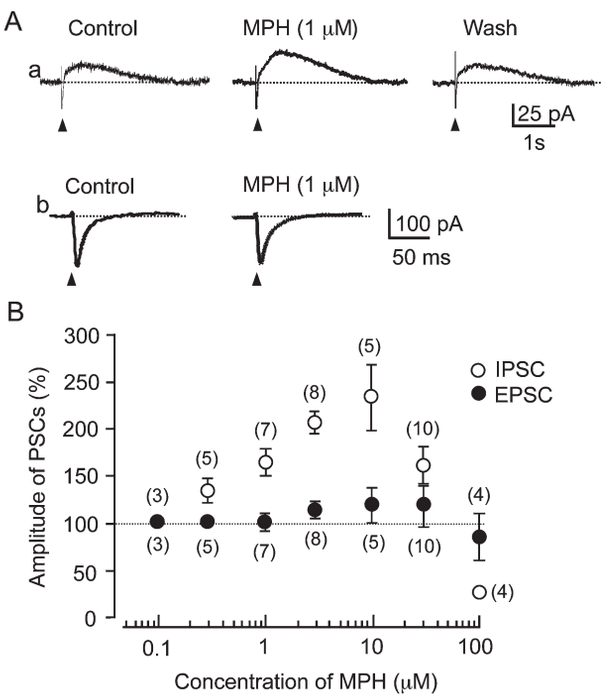

Fig. 2. Whole-cell patch-clamp studies of the effects of MPH (1 μM) on postsynaptic currents (PSCs). (A) Examples of the effects of MPH (1 μM) on the IPSC (a) and the EPSC (b) in LC neuron voltage-clamped at −60 mV. In records (a), left and middle records were obtained before and 10 min after application of MPH (1 μM), respectively. Right record was obtained 30 min after withdrawal of MPH (1 μM). Each trace was the sum of 3 responses. In records (b), left and right records were obtained before and 10 min after application of MPH. Each trace was the sum of 3 responses. (B) Concentration-response curves for MPH (0.1-100 μM) on the IPSC (○) and the EPSCs (●). The amplitudes of the EPSC and the IPSC were indicated by closed and open circles, respectively. The amplitude of PSCs obtained before application of MPH is indicated as 100%. Vertical lines on data points indicate SE of mean. The number of experiments is shown in parentheses.

It has been demonstrated that the IPSC is composed of two components produced by NE and γ-aminobutyric acid (GABA) in adult rat LC neurons [24]. We, therefore, examined the effect of MPH (3 μM) on the IPSC in LC neurons treated with yohimbine (1 μM), a blocker of α_2-adrenoceptors (Fig. 4A). Bath-application of yohimbine (1 μM) for 20 min produced an inward current with amplitude of 11.3 pA (n=4) that lasted as long as yohimbine (1 μM) was present in the LC neurons of juvenile rats (see Fig. 6Ab). Yohimbine (1 μM) largely reduced the amplitude of the IPSC. Addition of MPH (3 μM) to an ACSF containing yohimbine (1 μM) did not enhance either the amplitude or duration of the IPSC at the same neuron. Figure 4B shows pooled data for the effects of MPH (3 μM) and yohimbine (1 μM) on the IPSC in juvenile rat LC neurons. The amplitudes of IPSCs were 27.6±1.7 pA (n=5) and 6.3±0.7 pA (n=5) in the absence and the presence of yohimbine (1 μM), respectively. The amplitude of the IPSCs was 6.8±1.0 pA (n=5) in the presence of

both MPH (3 μM) and yohimbine (1 μM) in the ACSF. Thus, MPH (3 μM) did not significantly enhance the IPSC in the presence of yohimbine ($p<0.1$). These results suggest that MPH preferentially enhances noradrenergic IPSCs in LC neurons of juvenile rats.

It has been demonstrated that bath-application of NE (1 μM) produced an outward current (I_{NE}) via α_2-adrenoceptors in adult rat LC neurons [19,21]. In the present study, we examined the effect of MPH (1 μM) on the I_{NE} induced by exogenously applied NE in juvenile rat LC neurons. The amplitude of the I_{NE} was 22 pA under whole-cell patch-clamp conditions (Fig. 5Aa). The I_{NE} reached its peak within 3 min after the beginning of application of NE and then recovered 10-15 min after withdrawal of NE. At the same neuron, addition of MPH (1 μM) to the ACSF enhanced the I_{NE} to 48 pA (Fig. 5Ab). The time course of the I_{NE} was also markedly increased by MPH (10 μM). Bath-application of yohimbine (1 μM) for 20 min almost completely suppressed the I_{NE} (Fig. 5Ac). Figure 5B shows pooled data for the effects of yohimbine (1 μM) and MPH (1 and 10 μM) on the I_{NE} in juvenile rat LC neurons. Yohimbine (1 μM) depressed the I_{NE} to 23±3% (n=5, $p<0.01$) of control. MPH, at concentrations of 1 and 10 μM, increased the amplitude of the I_{NE} to 238±31% (n=7) and 261±20% (n=7) of control, respectively. These results suggest that MPH postsynaptically enhances the IPSC, probably by increasing the concentration of NE at noradrenergic synapses in the LC.

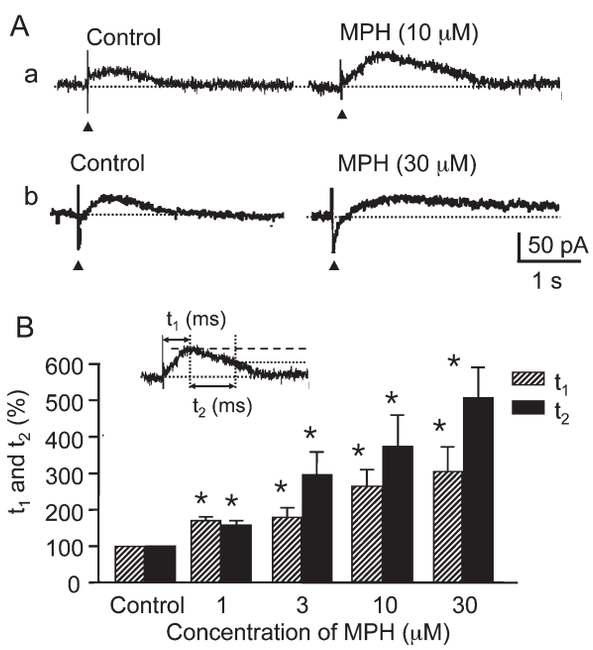

Fig. 3. Effects of MPH (1-30 μM) on the duration of the IPSC in juvenile rat LC neurons. (A) Examples of the effects of MPH 10 μM (a) and 30 μM (b) on the IPSC. Left and right records were obtained before and 10 min after application of MPH. (B) Graph shows the effect of MPH (1-30 μM) on the time course of the IPSC induced by MPH (1-30 μM). Inset shows the time-to-peak (t_1) and the half-decay time (t_2). The (t_1) and (t_2) obtained before application of MPH were indicated as 100% (control). Vertical lines on these columns indicate the mean±SE of mean. Asterisk indicates the statistical significance obtained by unpaired Student's *t*-test (*$p<0.01$ vs control). Each column was obtained from 6 cells.

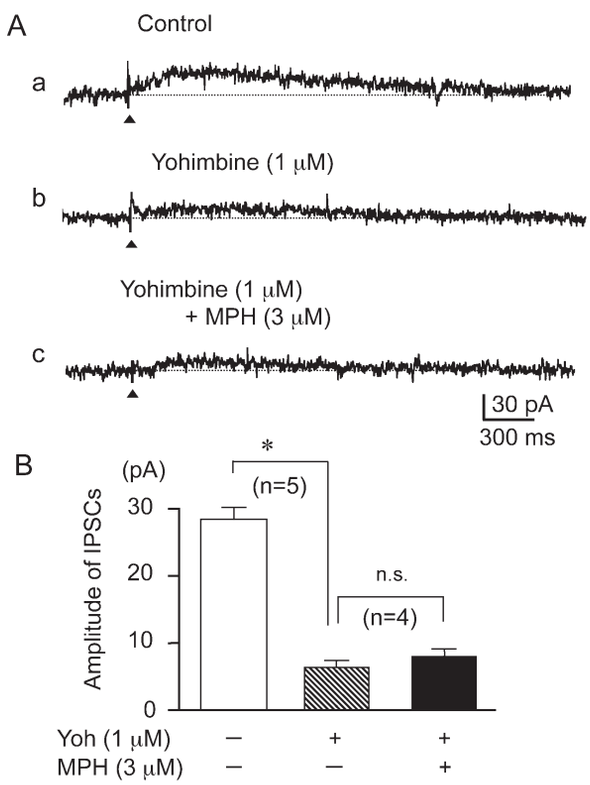

Fig. 4. Effects of yohimbine and MPH on the IPSC in juvenile rat LC neurons. (A) Records (a) and (b) were obtained before and 20 min after bath-application of yohimbine (1 μM), respectively. Record (c) was obtained in the presence of both yohimbine (1 μM) and MPH (3 μM). (B) Pooled data for the effects of yohimbine on the IPSC. The IPSC obtained before application of yohimbine (1 μM) is depicted as 100% (open column). Hatched and closed columns were obtained in the presence of yohimbine (1 μM) alone and both yohimbine (1 μM) and MPH (3 μM), respectively. Vertical lines on these columns indicate the mean±SE of mean. Asterisk indicates the statistical significance obtained by unpaired Student's *t*-test (*$p<0.01$ vs control). The n.s. indicates no statistical significance. The number of experiments is shown in parentheses.

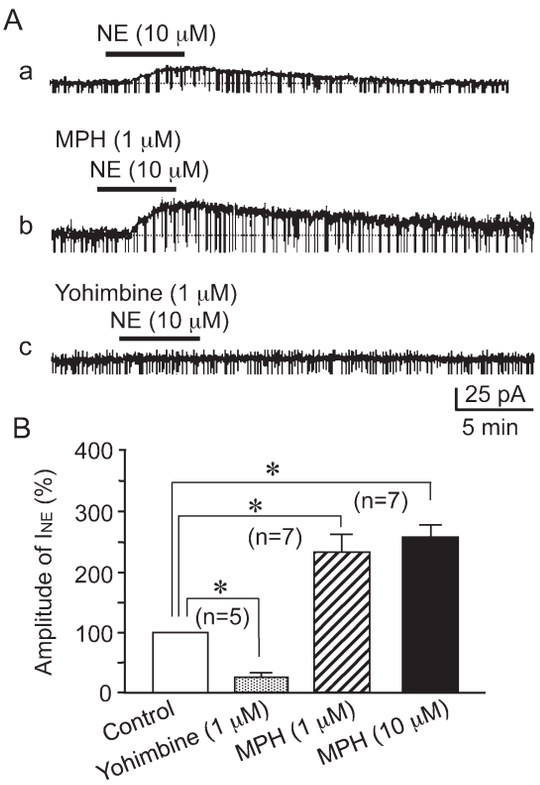

Fig. 5. Effects of yohimbine and MPH on the I_{NE} in juvenile rat LC neurons. (A) Record (a) and (b) were obtained before and 10 min after application of MPH (1 μM), respectively. Record (c) was obtained 20 min after application of yohimbine (1 μM) in the ACSF. Solid bars indicate the period of bath-application of NE (10 μM). (B) Pooled data for the effects of yohimbine and MPH (1 and 10 μM) on the I_{NE}. The I_{NE} obtained in the ACSF (open column) was indicated as 100%. Gray column was obtained in the presence of yohimbine (1 μM). Hatched and closed columns were obtained in the presence of MPH (1 μM) and (10 μM), respectively. Vertical lines on these columns indicate the mean±SE of mean. Asterisk indicates the statistical significance obtained by unpaired Student's *t*-test (*$p<0.01$ vs control). The number of experiments is shown in parentheses.

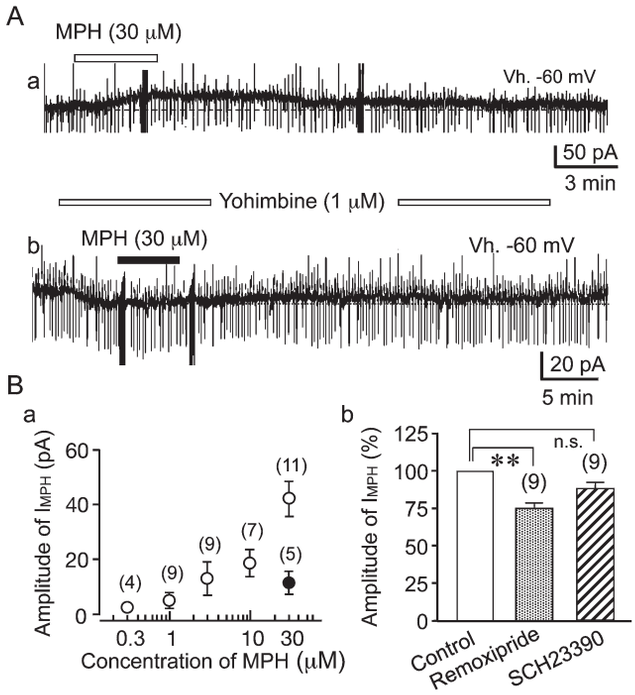

Fig. 6. Effect of yohimbine on the I_{MPH} in juvenile rat LC neurons. (A) Record (a) shows control I_{MPH} obtained at the holding membrane potential (Vh.) of −60 mV. Open horizontal bar indicates the period of bath-application of MPH (30 μM). Record (b) shows the effect of MPH (30 μM) on the membrane current in the presence of yohimbine (1 μM). Open and solid bars indicate the periods of bath-application of yohimbine (1 μM) and MPH (30 μM), respectively. The dot line indicates the peak of the yohimbine-induced inward current. (B) Graph (a) shows a concentration-response curve of the I_{MPH}. Open and closed circles were obtained in the absence and the presence of yohimbine (1 μM), respectively. Vertical line on each point indicates mean±SE of mean. Graph (b) shows pooled data for the effects of remoxipride (1 μM) and SCH23390 (1 μM) on the I_{MPH}. Open columns show control amplitude of the I_{MPH} obtained in the ACSF. Gray and hatched columns were obtained in the presence remoxipride (1 μM) and SCH23390 (1 μM), respectively. Vertical lines on columns indicate mean±SE of mean. The number of experiments is shown in parentheses. The n.s. indicates no statistical significance.

Properties of I_{MPH} mediated by NE in juvenile rat LC neurons

It has been shown that MPH causes an outward current (I_{MPH}) in LC neurons of adult rats [19]. Figure 6A shows the pharmacological properties of the I_{MPH} obtained in juvenile rat LC neurons under whole-cell patch-clamp conditions. The amplitude of the I_{MPH} was concentration-dependent (Fig. 6Ba). MPH (0.3-1 μM) produced no detectable outward current in 15 LC neurons. At a concentration of 3 μM, MPH produced the I_{MPH} with an amplitude of 14.8±5.1 pA (n=9) at −60 mV. The amplitudes of the I_{MPH} induced by MPH, 10 and 30 μM, were 17.2±2.8 pA (n=7) and 43.4±4.2 pA (n=11), respectively. Figure 6Ab shows an example of the effect of yohimbine (1 μM) on the I_{MPH} in a juvenile rat LC neuron. In the presence of yohimbine (1 μM), the application of MPH (30 μM) produced no

obvious outward current at the same LC neuron. In the presence of yohimbine (1 μM), the amplitude of the I_{MPH} produced by 30 μM MPH was 10.5±3.4 pA (n=5) (Fig. 6Ba, ●). Thus, yohimbine (1 μM) depressed the outward current induced by MPH (30 μM) to 74±5% (n=6) of control in juvenile rat LC neurons. Since MPH has been known to inhibit the re-uptake of DA in the CNS [10,11], it is possible that I_{MPH} may be mediated by DA in juvenile rat LC neurons. Figure 6Bb shows the effects of antagonists for D_1 and D_2 receptors on the I_{MPH} in juvenile rat LC neurons. The amplitude of the I_{MPH} was reduced to 75±4% (n=9) of control in the presence of remoxipride (1 μM), an antagonist for D_2 dopamine receptors. The depression of I_{MPH} by remoxipride (1 μM) was statistically significant as compared with those obtained in the absence of MPH ($p<0.05$). However, the amplitude of the I_{MPH} was 86±5% (n=9) of control in the presence of SCH23390 (1 μM), a D_1 receptor antagonist ($p<0.1$, vs. control). These data are not statistically different from those in control animals, suggesting that the I_{MPH} is mainly mediated by NE in juvenile rat LC neurons.

It has been demonstrated that the I_{MPH} is mediated by the inward rectifier K^+ current in adult rat LC neuron [19]. We, therefore, investigated the electrophysiological properties of the I_{MPH} in juvenile rat LC neurons. The I_{MPH} was associated with an increase in the membrane conductance (Fig. 7Ab). Figure 7Ba shows current-voltage (I-V) curves constructed by applying depolarizing and hyperpolarizing step-command potentials with a duration of 400 ms. The I-V curve obtained in the presence of MPH (30 μM) increased in slope and intersected the control curve at −91.1±4.3 mV (n=5). The reversal potential of the I_{MPH} is close to the equilibrium potential of K^+ channels in juvenile rat LC neurons. Figure 7Bb shows the net component of the I_{MPH} (▲) obtained by subtraction of the control I-V curve obtained in the ACSF (●) from that obtained in the presence of MPH (30 μM, ○). The net I_{MPH} exhibited inward rectification. It has been reported that Ba^{2+}, at a micromolar concentration, selectively blocks the inward rectifier K^+ current in various central neurons [25]. Application of Ba^{2+} (100 μM) itself produced an inward current at −60 mV in a juvenile rat LC neuron. In the presence of Ba^{2+} (100 μM), application of MPH (30 μM) did not produce an outward current at −60 mV (Fig. 7Ca). Pooled data showed that Ba^{2+} (100 μM) depressed the I_{MPH} to 23±4% (n=5) of control at −150 mV (Fig. 7Cb). These data suggest that I_{MPH} is mainly produced by activation of Ba^{2+}-sensitive inward rectifier K^+ conductance in LC neurons.

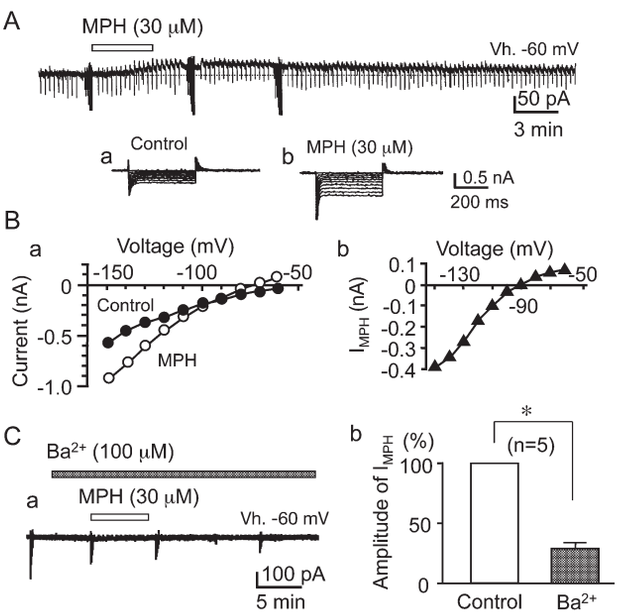

Fig. 7. Electrophysiological properties of the I_{MPH} in juvenile rat LC neurons. (A) Sample records of the I_{MPH} obtained by 30 μM MPH. Open horizontal bar indicate the period of the bath-application of MPH (30 μM). Lower records show inward current induced by hyperpolarizing command potentials with duration of 400 ms. Records (a) and (b) were obtained before and 10 min after application of MPH (30 μM), respectively. (B) Graph (a) shows I-V curves obtained before (●) and during (○) the application of MPH (30 μM). Data were obtained from upper record (A). Graph (b) shows net I_{MPH} (▲) obtained by subtraction of the control curve from that obtained in the presence of MPH (30 μM) in graph (a). (C) Effect of Ba^{2+} (100 μM) on the I_{MPH} in juvenile rat LC neurons. Record (a) shows sample membrane current obtained in the presence of both Ba^{2+} (100 μM) and MPH (30 μM). Graph (b) shows pooled data for the effect of Ba^{2+} on the I_{MPH}. Open and hatched columns were obtained before and 10 min after application of Ba^{2+} (100 μM). Vertical line on the hatched column indicate the mean±SE of mean. Asterisk indicates the statistical significance obtained by unpaired Student's *t*-test (*$p<0.01$). The number of experiments is shown in parentheses.

DISCUSSION

The present study showed that bath-application of MPH (0.1-10 μM) enhanced the IPSP (and IPSC) in a concentration-dependent manner in juvenile rat LC neurons. MPH (1-30 μM) also increased the duration (time-to-peak and half-decay-time) of the IPSC. In contrast, the EPSP (and EPSC) was not significantly changed by MPH (0.3-100 μM). It has been shown that the EPSP is mediated by excitatory amino acids,

while the IPSP is mediated by NE in LC neurons of adult rats [21]. Thus, MPH selectively enhances the inhibitory noradrenergic transmission in juvenile rat LC neurons. These results are comparable to those in LC neurons of adult rats. It has been shown that the IPSP is composed of two current components mediated by NE and GABA in mammalian LC neurons [24]. Bath-application of yohimbine (1 μM), an α_2-adrenoceptor antagonist [26], strongly reduced the amplitude of the IPSC in LC neurons of juvenile rats. In the presence of yohimbine (1 μM), application of MPH (3 μM) to LC neurons did not obviously enhance the residual IPSC. The NE-induced outward current (I_{NE}) was clearly enhanced by MPH (1 μM). Furthermore yohimbine (1 μM) blocked the I_{NE}. These results suggest that the NE component of the IPSP is preferentially enhanced via activation of α_2-adrenoceptors. It is, therefore, concluded that MPH enhances IPSP by increasing the concentration of intrinsic NE at noradrenergic synapses in juvenile rat LC neurons.

Whole-cell patch-clamp studies also showed that bath-application of MPH (1-30 μM) directly produced an outward current (I_{MPH}) in juvenile rat LC neurons. Yohimbine (1 μM) strongly depressed the I_{MPH}. Since MPH has been known to block not only NET but also DAT in the mammalian CNS [10,11,27], the contribution of DA to the I_{MPH} was examined in juvenile rat LC neurons. The I_{MPH} was significantly depressed by remoxipride, a D_2 receptor antagonist, but not by SCH23390, a D_1 receptor antagonist. These results suggest that DA is marginally involved in the I_{MPH}. A recent HPLC study showed that DA content was 5 times lower than that of NE in LC neurons [28]. Thus, NE may be the primary mediator of the MPH-induced hyperpolarizing response (and the I_{MPH}) in the juvenile rat LC. The amplitude of the I_{MPH} was increased at hyperpolarizing membrane potentials, showing inward rectification. The I_{MPH} reversed polarity near the equilibrium potential of K^+ ions. The I_{MPH} was strongly depressed by Ba^{2+} (100 μM), a selective blocker for the inward rectifier K^+ current in the CNS [25]. In the present study, application of Ba^{2+} (100 μM) itself produced an inward current at −60 mV in the ACSF and blocked the I_{MPH}. These results suggest that the I_{MPH} is produced by activation of Ba^{2+}-sensitive inward rectifier K^+ current in juvenile rat LC neurons. Similar properties of the I_{MPH} were shown in adult rat LC neurons [19].

It has been reported that catecholamine content is detected in the LC neurons by 1 week after birth [29]. Recent studies have shown that the LC has very high expression of NET in the early postnatal period (5-20 postnatal day) and that the NET level in the LC exceeded the highest values found in any region in the CNS at an early developmental period [30]. NE is tonically released from recurrent collaterals of noradrenergic LC neurons [21]. In the present study, application of yohimbine itself to LC neurons in the juvenile rat caused an inward current at −60 mV. These results suggest that yohimbine blocks the outward current induced by intrinsic NE in juvenile rat LC neurons. In the present study, we observed that MPH produced a bell-shaped concentration-response relationship in enhancing the IPSC. MPH, at a concentration between 0.3 and 10 μM, increased the amplitude of the IPSC in a concentration-dependent manner. However, the effect of MPH (30 μM) was less potent than MPH (10 μM) in enhancing the IPSC. The IPSC was strongly depressed by MPH (100 μM). Since the IPSC and the I_{MPH} are mediated by the same α_2-adrenoceptors, bath-application of MPH (30-100 μM) prior to nerve stimulation interferes with the action of nerve-evoked NE at the same noradrenergic synapses. In addition to the postsynaptic mechanism, the increase in NE content by MPH (30-100 μM) should activate presynaptic α_2-autoreceptors, resulting in the blockade of the release of NE [31].

LC neurons in the juvenile rat exhibited tonic firing of spontaneous action potentials with a frequency of 0.5 to 3 Hz at the resting membrane potential, resembling those in adult rat LC neurons [21]. The frequency of spontaneous firing activity appeared to be depressed during the application of MPH in juvenile rat LC neurons. The MPH-induced hyperpolarization and enhancement of the time course of the IPSP should depress the rate of output signals from the LC to various projection neurons in the CNS. It has been demonstrated that the firing rate of spontaneous action potentials is a pacemaker-like regulatory activity in the LC neurons [32]. Aston-Jones et al. [33] have proposed that noradrenergic neurons in the LC have two distinguishable modes of activity, namely phasic and tonic discharges of LC neurons. The tonic discharge activity mode may be related to search for alternative behavior, while phasic mode of LC activity may reinforce behaviors and help optimize task performance [34,35]. Previous studies with extracellular recording methods reported that intravenous or intraperitoneal administration of MPH decreased the spontaneous firing rate in adult rat LC neurons [16,18]. Decrement of tonic activity by MPH in LC neurons may change the discharge rate of LC neurons from a tonic to phasic mode of activity, improving attentional task performance.

The medial PFC is implicated in the formation of

many cognitive functions including arousal, selective attention, and short-term working memory [4,34,36]. Activation of noradrenergic neurons in the PFC facilitates cognitive function [37], attentional performance, learning and memory [38,39]. In contrast, the reduction of NE release by activation of presynaptic α_2-autoreceptors in adrenergic synapses produces deleterious effects on attention and target detection [8,9]. In contrast, MPH, by increasing NE content in the PFC, improves the working memory and attentional functions in rats, while reducing locomotor activity [35]. A recent study has shown that MPH, at low concentrations, preferentially increases catecholamine neurotransmission within the PFC and enhances cognitive function [12]. MPH reduces the firing rate of spontaneous activity by enhancement of noradrenergic synapses, and increases the signal-to-noise ratio of incoming neuronal activities, making excitatory synaptic transmission more effective in the PFC. Further studies are needed to clarify whether the enhancement of noradrenergic inhibition in LC and/or PFC neurons underlies the therapeutic mechanism of MPH in patients with ADHD.

ACKNOWLEDGMENTS: This work was supported by a Grant-in-Aid for Young Scientists (B) (17790735) and by a project to promote establishment of open research centers in private universities sponsored by the Ministry of Education, Culture, Sports, Science and Technology of Japan.

REFERENCES

1. Seeman P, and Madras B. Methylphenidate elevates resting dopamine which lowers the impulse-triggered release of dopamine: a hypothesis. Behav Brain Res 2002; 130:79-83.
2. Solanto MV. Neuropsychopharmacological mechanisms of stimulant drug action in attention-deficit hyperactivity disorder: a review and integration. Behav Brain Res 1998; 94:127-152.
3. Ferguson SA. A review of rodent models of ADHD. In: Stimulant Drugs and ADHD, Basic and Clinical Neuroscience, ed. Solanto MV, Arnsten AFT, and Castellanos FX, Oxford University Press, New York, pp 209-220, 2001.
4. Arnsten AFT. Stimulants: therapeutic actions in ADHD. Neuropsychopharmacology 2006; 31:2376-2383.
5. Pliszka SR, McCracken JT, and Maas JW. Catecholamines in attention-deficit hyperactivity disorder: current perspectives. J Am Acad Child Adolesc Psychiatry 1996; 35:264-272.
6. Popper CW. Pharmacologic alternatives to psychostimulants for the treatment of attention-deficit/hyperactivity disorder. Child Adolesc Psychiatr Clin N Am 2000; 9:605-646.
7. Scahill L, Chappell PB, Kim YS, Schultz RT, Katsovich L et al. A placebo-controlled study of guanfacine in the treatment of children with tic disorders and attention deficit hyperactivity disorder. Am J Psychiatry 2001; 158:1067-1074.
8. Coull JT, Jones MEP, Egan TD, Frith CD, and Maze M. Attentional effects of noradrenaline vary with arousal level: selective activation of thalamic pulvinar in humans. NeuroImage 2004; 22:315-322.
9. Smith A, and Nutt D. Noradrenaline and attention lapses. Nature 1996; 380:291.
10. Biederman J, and Spencer T. Attention-deficit/hyperactivity disorder (ADHD) as a noradrenergic disorder. Biol Psychiatry 1999; 46:1234-1242.
11. Davids E, Zhang K, Tarazi FI, and Baldessarini RJ. Animal models of attention-deficit hyperactivity disorder. Brain Res Rev 2003; 42:1-21.
12. Berridge CW, Devilbiss DM, Andrzejewski ME, Arnsten AFT, Kelley AE et al. Methylphenidate preferentially increases catecholamine neurotransmission within the prefrontal cortex at low doses that enhance cognitive function. Biol Psychiatry 2006; 60:1111-1120.
13. Amaral DG, and Sinnamon HM. The locus coeruleus: neurobiology of a central noradrenergic nucleus. Prog Neurobiol 1977; 9:147-196.
14. Moore RY, and Bloom FE. Central catecholamine neuron systems: anatomy and physiology of the norepinephrine and epinephrine systems. Annu Rev Neurosci 1979; 2:113-168.
15. Foote SL, Aston-Jones G, and Bloom FE. Impulse activity of locus coeruleus neurons in awake rats and monkeys is a function of sensory stimulation and arousal. Proc Natl Acad Sci USA 1980; 77:3033-3037.
16. Olpe HR, Steinmann MW, and Jones RSG. Locus coeruleus as a target for psychogeriatric agents. Ann NY Acad Sci 1985; 444:394-405.
17. Aston-Jones G, Rajkowski J, and Cohen J. Role of locus coeruleus in attention and behavioral flexibility. Biol Psychiatry 1999; 46:1309-1320.
18. Lacroix D, and Ferron A. Electrophysiological effects of methylphenidate on the coeruleo-cortical noradrenergic system in the rat. Eur J Pharmacol 1988; 149:277-285.
19. Ishimatsu M, Kidani Y, Tsuda A, and Akasu T. Effects of methylphenidate on the membrane potential and current in neurons of the rat locus coeruleus. J Neurophysiol 2002; 87:1206-1212.
20. Kidani Y, Ishimatsu M, Kuwahata T, Yamashita Y, Akasu T et al. Effects of milnacipran on neuronal excitability and synaptic transmission in neurons of the rat locus coeruleus. No To Hattatsu 2005; 37:31-38. (in Japanese)
21. Egan TM, Henderson G, North RA, and Williams JT. Noradrenaline-mediated synaptic inhibition in rat locus coeruleus neurones. J Physiol 1983; 345:477-488.
22. Kidani Y, Ishimatsu M, Kuwahata T, and Akasu T. Methylphenidate enhances the noradrenergic effects on locus coeruleus neurons of the juvenile rat. Jpn J Physiol 2004; 54:S149.
23. Ishimatsu M, and Williams JT. Synchronous activity in locus coeruleus results from dendritic interactions in pericoerulear regions. J Neurosci 1996; 16:5196-5204.
24. Surprenant A, and Williams JT. Inhibitory synaptic potentials recorded from mammalian neurones prolonged by blockade of noradrenaline uptake. J Physiol 1987; 382:87-

103.
25. North RA. Drug receptors and the inhibition of nerve cells. Br J Pharmacol 1989; 98:13-28.
26. Williams JT, Henderson G, and North RA. Characterization of α_2-adrenoceptors which increase potassium conductance in rat locus coeruleus neurones. Neuroscience 1985; 14:95-101.
27. Hendley ED, and Fan XM. Regional differences in brain norepinephrine and dopamine uptake kinetics in inbred rat strains with hypertension and/or hyperactivity. Brain Res 1992; 586:44-52.
28. Ikeura S, Kidani Y, Ishimatsu M, and Akasu T. Norepinephrine content was increased in locus coeruleus and medial prefrontal cortex of spontaneously hypertensive rats (SHR), AD/HD model rat. J Physiol Sci 2006; 56: S173.
29. Maeda T, and Gerebtzoff MA. On the development of locus ceruleus. 2. Histoenzymatic study. Acta Neurol Psychiatr Belg 1969; 69:11-19.
30. Sanders JD, Happe HK, Bylund DB, and Murrin LC. Development of the norepinephrine transporter in the rat CNS. Neuroscience 2005; 130:107-117.
31. Curet O, and de Montigny C. Electrophysiological characterization of adrenoceptors in the rat dorsal hippocampus. Ⅲ. Evidence for the physiological role of terminal α_2-adrenergic autoreceptors. Brain Res 1989; 499:18-26.
32. Williams JT, and North RA. Catecholamine inhibition of calcium action potentials in rat locus coeruleus neurones. Neuroscience 1985; 14:103-109.
33. Aston-Jones G, Rajkowski J, Kubiak P, and Alexinsky T. Locus coeruleus neurons in monkey are selectively activated by attended cues in a vigilance task. J Neurosci 1994; 14:4467-4480.
34. Aston-Jones G, Rajkowski J, and Cohen J. Locus coeruleus and regulation of behavioral flexibility and attention. Prog Brain Res 2000; 126:165-182.
35. Aston-Jones G, and Cohen JD. An integrative theory of locus coeruleus-norepinephrine function: adaptive gain and optimal performance. Annu Rev Neurosci 2005; 28:403-450.
36. Dalley JW, Cardinal RN, and Robbins TW. Prefrontal executive and cognitive functions in rodents: neural and neurochemical substrates. Neurosci Biobehav Rev 2004; 28:771-784.
37. Lapiz MDS, and Morilak DA. Noradrenergic modulation of cognitive function in rat medial prefrontal cortex as measured by attentional set shifting capability. Neuroscience 2006; 137:1039-1049.
38. Bunsey MD, and Strupp BJ. Specific effects of idazoxan in a distraction task: evidence that endogenous norepinephrine plays a role in selective attention in rats. Behav Neurosci 1995; 109:903-911.
39. Devauges V, and Sara SJ. Activation of the noradrenergic system facilitates an attentional shift in the rat. Behav Brain Res 1990; 39:19-28.

Case Report

Kurume Medical Journal, 57, 39-41, 2010

A Case of Brain Metastasis from Pulmonary Giant Cell Carcinoma

NAOSHI HAGIHARA, TOSHI ABE*, TOMIHIRO WAKAMIYA, YASUO SUGITA**, MITSUO WATANABE AND KAZUO TABUCHI

Department of Neurosurgery, Koyanagi Memorial Hospital, Saga 840-2195 and Departments of Radiology and Pathology**, Kurume University School of Medicine, Kurume 830-0011, Japan*

Received 24 September 2009, accepted 22 January 2010

Edited by HISAMICHI AIZAWA

Summary: A 74-year old female was admitted to our hospital due to sudden right hemiparesis. Precontrast brain computed tomography (CT) revealed multiple high-density masses consistent with multiple hemorrhage, and chest CT scan demonstrated a mass in the left lung field without hemorrhage. Follow-up CT showed enlargement of the multiple intracerebral hemorrhages. A diagnosis was made of brain metastasis from a rare pure giant cell carcinoma (GCC) of the lung.

Key words brain metastasis, pulmonary giant cell carcinoma, multiple hemorrhage

INTRODUCTION

The World Health Organization classification of lung carcinoma ranks the heterogeneous non-small cell lung cancer group, encompassing sarcoma or sarcoma-containing tumors under one heading: "carcinomas with pleomorphic, sarcomatoid or sarcomatous elements" [1]. This group contains entities such as pleomorphic carcinoma, spindle cell carcinoma, giant cell carcinoma (GCC), carcinosarcoma and pulmonary blastoma. These tumors are rare overall, making up approximately 0.1-0.4% of all lung malignancies [2].

CASE REPORT

A 74-year old female was admitted to our hospital due to sudden right hemiparesis. Neurological examination revealed mild hemiparesis of the right extremities. Precontrast brain computed tomography (CT) revealed multiple high-density masses consistent with multiple hemorrhage (Fig. 1). Magnetic resonance (MR) imaging detected all the hematoma at high signal intensity because of bleeding accompanied by ring enhancement with Gadolinum. Contrast enhanced chest CT scan demonstrated a mass in the left lung field without hemorrhage (Fig. 2). Laboratory data showed mild elevation of LDH (282 IU/L), IL-2R (538 U/ml) and NSE (52 ng/ml). Bleeding and coagulation times were within normal range. After admission, the patient was kept in bed and monitored closely. Blood pressure remained within normal range without medication. At first, the cerebral hemorrhage was treated conservatively. She gradually became drowsy and right hemiparesis progressed. Follow-up CT, 7 days after admission, revealed enlargement of all hematoma. As a result, we performed evacuation of the hematomas and biopsy of the left frontal lobe lesion via a left frontal craniotomy. Histological examination identified the lesion as a pure GCC (Fig. 3). Immunohistochemically, cytokeratin AE1/E3 was positive, but CK7, CK20, thyroid transcription factor-1, and glial fibrillary acidic protein were negative. In addition to Hematoxilin-eosin staining, these immunostaining findings are consistent with GCC. The diagnosis was made of brain metasta-

Address for correspondence: Naoshi Hagihara, M.D., Department of Neurosurgery, Koyanagi Memorial Hospital, 230-2 Morodomitsu, Morodomi-cho, Saga city, Saga 840-2195, Japan. Tel: 81-952-47-3255 Fax: 81-952-47-5101 E-mail: hagihare167@solid.ocn.ne.jp

Abbreviations: CT, computed tomography; GCC, giant cell carcinoma; MR, magnetic resonance.

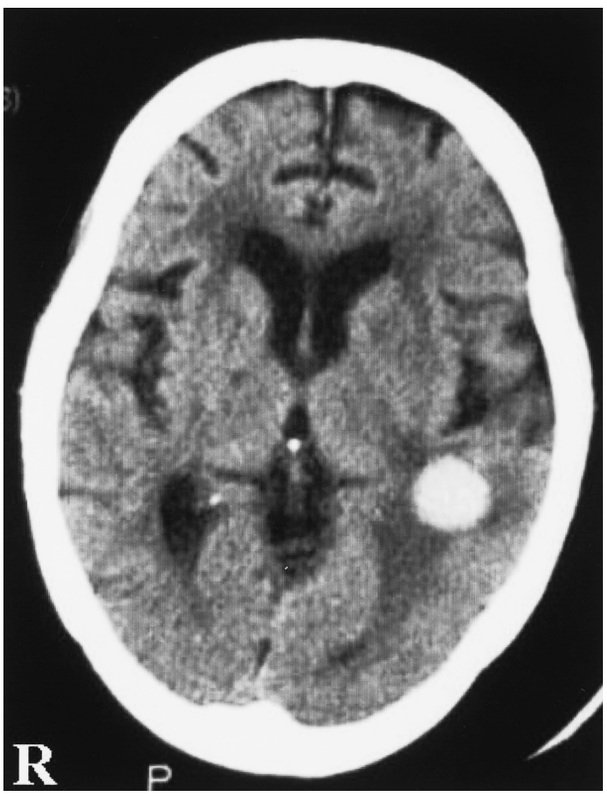

A

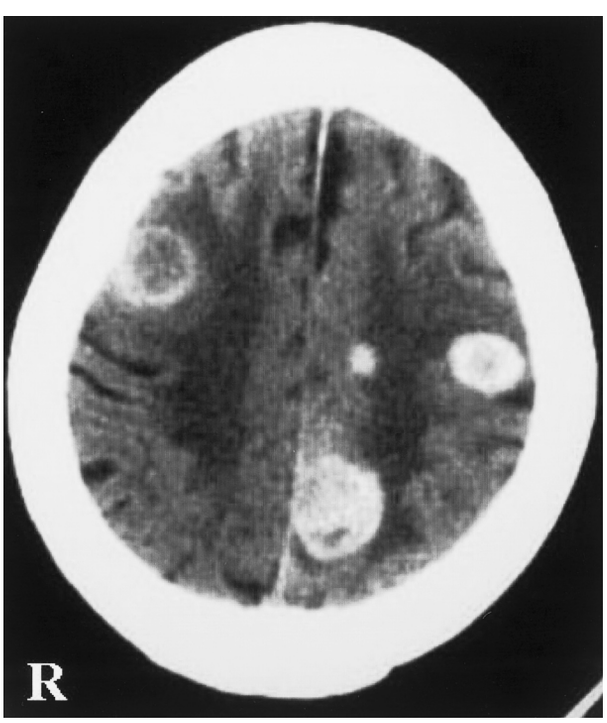

B

Fig. 1. Brain CT shows multiple hemorrhagic mass lesions in the cortico-medullary junction.

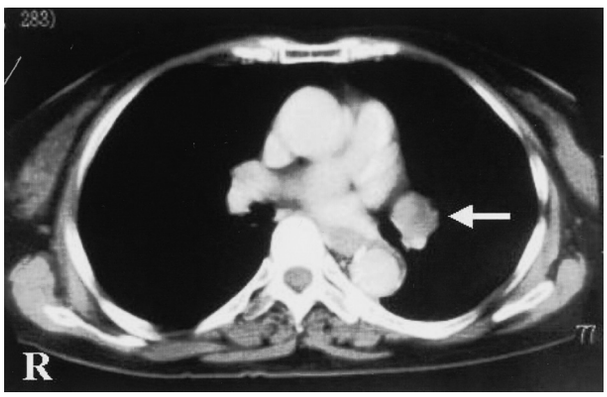

Fig. 2. Contrast enhanced chest CT showed pulmonary mass at left hilum.

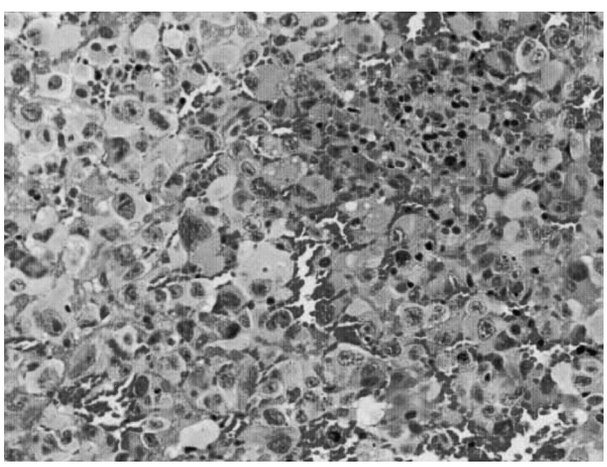

Fig. 3. Pathological findings of the brain around hematoma in the left frontal lobe. The section consisited of a diffuse proliferation of atypical giant cells. No sarcomatoid component was seen.

sis from lung GCC. Since the patient failed to recover consciousness we recommended against performing adjuvant therapy. The follow-up CT series revealed remarkable enlargement of the hematomas, especially in the left cerebellum. Unfortunately, one month after admission she died of progressive prostration.

DISCUSSION

This is a case of brain metastasis from a rare pulmonary GCC. Pulmonary GCC in particular is generally regarded as a distinct entity based on its unusual histologic features and its extremely aggressive clinical course [3,4]. This case demonstrated multiple intracerebral hemorrhages with remarkable enlargement in a short period. There are some reports of intratumoral

hemorrhage associated with brain metastasis from lung cancer. However, simultaneous hemorrhage of multiple metastatic lesions is uncommon. In general we should consider brain tumor, along with hypertension, trauma, amyloid angiopathy, hemorrhagic infarction, hematologic disorder, liver disease and drugs, as possible causes of multiple intracerebral hemorrhage. Among metastatic brain tumors, malignant melanomas as well as choriocarcinoma and renal cell carcinomas frequently develop significant hemorrhages. With regard to etiology, the causes of intratumoral hemorrhage are often considered to be endothelial proliferation with vascular obliteration, vessel compression and distortion due to rapid tumor growth, vessel necrosis, invasion of vessel walls by the tumor, and increased venous pressure associated with increased intracranial pressure [5,6]. In some cases, hypertension and coagulopathy are thought to be risk factors of intratumoral hemorrhage. Similar mechanisms, i.e. aggressive invasion and neovascularity of GCC, are likely to be associated with the multiple intracerebral hemorrhages in this case. Moreover, in spite of bed rest, medication with hemostatic drugs and the absence of high blood pressure or abnormalities in the coagulating system, a remarkable enlargement of the hematomas occurred in a short period.

Intracerebral multiple metastases were detected with hemorrhage, but the primary lung GCC was detected without bleeding in our case. Shoji et al. [7] reported a case of small intestinal metastases with bleeding 6 days prior to the discovery of bleeding from a primary lung GCC. We speculate that both the primary and metastatic lesions have an equally strong tendency to bleed. Lung carcinoma often metastasizes to the brain. Although adjuvant therapies such as radiation and chemotherapy are often performed in addition to surgical resection, the prognosis is still poor. Shoji et al. [7] reported a rare case of stage IV (without brain metastasis) pulmonary GCC who has survived long-term after undergoing aggressive surgical treatment and chemotherapy. However chemotherapy for brain metastasis from pulmonary GCC is unlikely to be effective due to problems with drug delivery. We should consider metastatic brain tumor as a possible cause in cases of multiple intracerebral hemorrhage. In this case, we were able to easily detect lung carcinoma on chest CT. However, because metastatic lesions from GCC have a tendency to bleed [7], intracerebral hemorrhage might be discovered before the detection of lung carcinoma in some cases.

REFERENCES

1. Travis WD, Colby TV, Corrin B, Shimosato Y, and Brambilia E. World Health Organization International Histological Classification of Tumors. Histological typing of Lung and Pleural Tumors. 3rd edition. Berlin: Springer Verlag; 1999.
2. Brambilia E, Travis WD, Colby TV, Corrin B, and Shimosato Y. The new World Health Organization classification of lung tumors. Eur Respir 2001; 18:1059-1068.
3. Shin MS, Jackson LK, Shelton, Jr RW, and Greene RE. Giant cell carcinoma of the lung. Clinical and roentgenographic manifestations. Chest 1986; 89:366-369.
4. Zhao ZL, Song N, Huang QY, Liu YP, and Zhao HR. Clinicopathologic features of lung pleomorphic (spindle/giant cell) carcinoma-A report of 17 cases. Ai Zheng 2007; 26:183-188.
5. Hirano A, and Matsui T. Vascular structures in brain tumors. Human Pathol 1975; 6:611-621.
6. Kondziolka D, Bernstein M, Resch L, Tator CH, Fleming JF et al. Significance of hemorrhage into brain tumors: clinicopathological study. J Neurosurg 1987; 67:852-857.
7. Shoji F, Maruyama R, Okamoto T, Ikeda J, Nakamura T et al. Long-term survival after an aggressive surgical resection and chemotherapy for stage IV pulmonary giant cell carcinoma. World Journal of Surgical Oncology 2005; 3:32.